Progress in Materials Science 56 (2011) 109–138

Contents lists available at ScienceDirect

Progress in Materials Science

journal homepage: www.elsevier.com/locate/pmatsci

Size effects in foams: Experiments and modeling

C. Tekoğlu [a], L.J. Gibson [b], T. Pardoen [a], P.R. Onck [c,*]

[a] Institute of Mechanics, Materials and Civil Engineering, Université catholique de Louvain, Place Sainte Barbe 2, B-1348 Louvain-la-Neuve, Belgium
[b] Department of Materials Science and Engineering, Masachusetts Institute of Technology, Cambridge, USA
[c] University of Groningen, Micromechanics of Materials, Zernike Institute for Advanced Materials, Groningen, The Netherlands

A R T I C L E I N F O

Article history:
Received 27 April 2010
Accepted 31 May 2010

A B S T R A C T

Mechanical properties of cellular solids depend on the ratio of the sample size to the cell size at length scales where the two are of the same order of magnitude. Considering that the cell size of many cellular solids used in engineering applications is between 1 and 10 mm, it is not uncommon to have components with dimensions of only a few cell sizes. Therefore, both for mechanical testing and for design, it is important to understand the link between the cellular morphology and size effects, which is the aim of this study. In order to represent random foams, two-dimensional (2D) Voronoi tessellations are used, and four representative boundary value problems – compression, shear, indentation, and bending – are solved by the finite element (FE) method. Effective elastic and plastic mechanical properties of Voronoi samples are calculated as a function of the sample size, and deformation mechanisms triggering the size effects are traced through strain maps. The modeling results are systematically compared with experimental results from the literature. As a rule, with decreasing sample size, the effective macroscopic stiffness and strength of Voronoi samples decrease under compression and bending, and increase under shear and indentation. The physical mechanisms responsible for these trends are identified.

Contents

* Corresponding author. Tel.: +31 50 363 80 39; fax: +31 50 363 48 86.
E-mail address: p.r.onck@rug.nl (P.R. Onck).

0079-6425/$ - see front matter © 2010 Elsevier Ltd. All rights reserved.
doi:10.1016/j.pmatsci.2010.06.001

1. Introduction

The mechanical behavior of a cellular material depends on its relative density (typically raised to a power between 1 and 3), the properties of the cell wall material, and the cell geometry (i.e., the number, shape, and thickness of cell walls and faces). Moreover, the individual response of cells to a loading is strongly influenced by their location in the material: deformation of cells located in the bulk, surrounded by other cells, or located near the edges where kinematic boundary conditions are applied, are more constrained compared to cells adjacent to stress-free boundaries. If the length, width, and thickness of a foam sample are all large enough to include many cells, the differences in per-cell response to a macroscopic loading are averaged out, leading to size-independent effective properties. If, however, one of the structural dimensions contains only a few cells, as is the case in many practical applications, the effective response of the foam is dictated by the individual excitements of the cells, resulting in a size-dependent mechanical behavior.

Early experiments exploring size effects in foams date back to the 1980's. Lakes [1,2] showed that the bending and torsional rigidities increase with decreasing sample size, for an open- and a closed-cell polymeric foam, respectively. For an open-cell reticulated vitreous carbon foam, on the other hand, Brezny and Green [3] showed that both the Young's modulus and the bending strength decrease dramatically with decreasing sample size. Similarly, Anderson et al. [4] and Anderson and Lakes [5] observed a reduction with decreasing sample size in the bending and torsional rigidities of a closed-cell polymethacrylimide foam, and of an open-cell copper foam, respectively. Most of the other bending experiments for foams concern sandwich panels, where a foam core material separates two face sheets of dense solids (see e.g. Bart-Smith et al. [6,7], Crupi and Montanini [8]). The deformation and the failure mechanisms of sandwich panels strongly depend on the foam core thickness (see e.g. Styles et al. [9]).

Bastawros et al. [10] conducted compression tests on closed-cell aluminum foams (trade name Alporas; Shinko Wire, Amagasaki, Japan), and Andrews et al. [11] on both closed-cell Alporas and open-cell aluminum foams (Duocel; ERG, Oakland, CA). Both studies showed that the compressive stiffness and strength of these foams reduce with decreasing sample size. Jeon and Asahina [12] tested Alporas samples without structural defects – such as partially coupled cells, missing cells, and collapsed cells, normally observed in Alporas foams – andn showed that the Young's modulus decreases with decreasing sample size, although the compressive strength was found to be size-independent. Several other researchers investigated the deformation mechanisms in a variety of metal foams under compression (e.g. Bastawros et al. [10], Bart-Smith et al. [13], Dannemann and Lankford [14], Hakamada et al. [15], Park and Nutt [16], Wang et al. [17]); they all reported that deformation localizes in narrow bands.

An increase in shear stiffness and strength with decreasing sample size is observed for aluminum foams (e.g. Andrews et al. [11], for both Alporas and Duocel; Chen and Fleck [18], only for Alporas). Rakow and Waas [19] analyzed size effects and deformation mechanisms under shear for an aluminum foam produced by the melt route. They showed that the average shear strain is much larger for the cells located in the bulk than it is for the cells bonded to the rigid platens – through which the shear load is applied. Kesler and Gibson [20] conducted three-point bending experiments on sandwich panels with Alporas foam cores of different sizes, where the panels are designed to fail by core shear. They showed that the shear strength is a function of the specimen size.

Among many indentation experiments on foams (e.g. Stupak and Donovan [21], Prakash et al. [22], Kumar et al. [23], Ramachandra et al. [24], Ramamurty and Kumaran [25], Kádár et al. [26], Mohan et al. [27], Lu et al. [28]), only a few consider the effect of the indenter size on the mechanical response (e.g. Andrews et al. [11], Olurin et al. [29]). Both of the latter two studies concluded that the peak indentation stress for the closed-cell Alporas foams increases with decreasing indenter size. Experiments performed on different low relative density ($\rho \approx 0.1$–0.15) metal foams reported that the deformation localizes in the cells immediately beneath the indenter, while the cells in the other regions remain in pristine condition (e.g. Andrews et al. [11], Ramachandra et al [24], Ramamurty and Kumaran [25], Kádár et al. [26], Olurin et al. [29]).

Stress/strain concentrations due to notches and holes in foams have also been experimentally investigated. Antoniou et al. [30], for example, found that for uniaxial compression of Alporas foams, the net section strength increases with increasing net section width for double-edge-notched specimens, while it remains constant for single-edge-notched specimens. Mora and Waas [31] performed compression experiments on polycarbonate honeycombs made of circular cells, containing a circular cylindrical hole in the middle. They showed that the intensity of the strain concentration in the vicinity of the hole depends on the hole radius, relative to the cell size. Guo and Gibson [32] calculated the decrease in the Young's modulus and the compressive elastic buckling and plastic collapse stresses of a honeycomb with central voids of increasing size using finite element analysis.

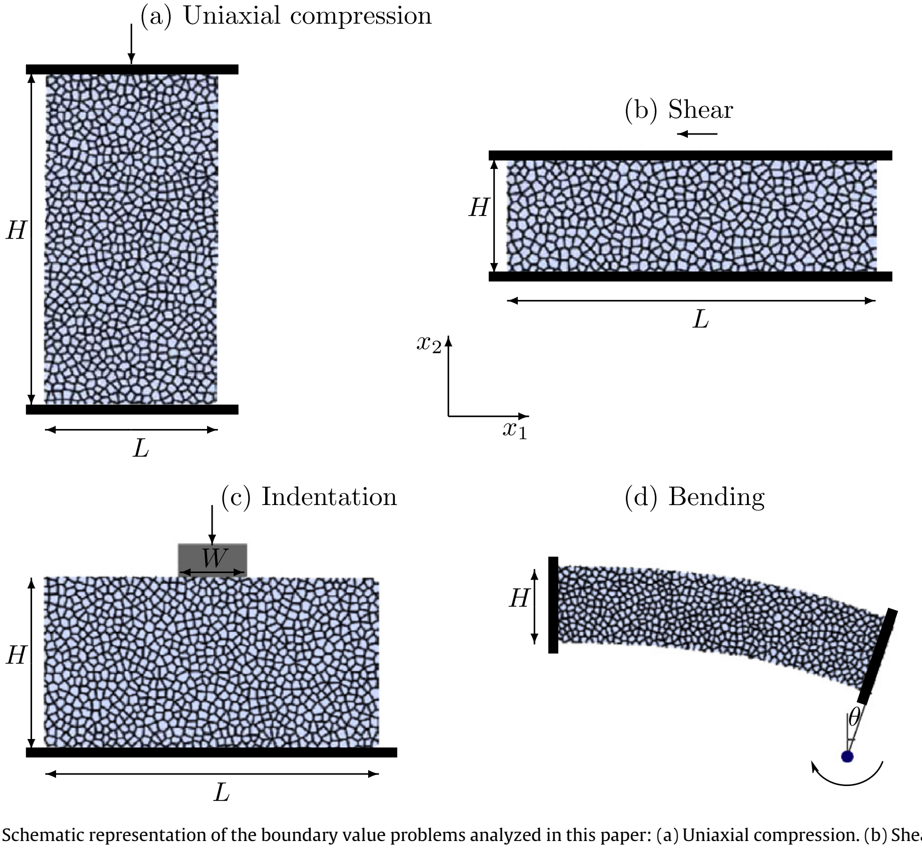

Fig. 1. Schematic representation of the boundary value problems analyzed in this paper: (a) Uniaxial compression. (b) Shear. (c) Indentation. (d) Bending. The cellular topology of real foams is mimicked by using 2D Voronoi tessellations.

The aim of this paper is to offer a wide appraisal of the origin of the size effects in the mechanical behavior of foams. For this purpose, the four most representative structural engineering problems, namely, compression, shear, indentation, and bending are addressed, where the cellular topology of real foams is mimicked by using 2D Voronoi tessellations (see Fig. 1). Section 2 introduces the numerical methods used in the paper. Section 3 presents the results: for each boundary value problem, elastic and plastic effective mechanical properties are given as a function of the sample size, as well as presenting strain maps that show the deformation mechanisms. The results of the Voronoi model are also compared with experimental results on metal foams.[1] Section 4 discusses the results, and attempts to build a link between the cellular morphology and the size effects, while the capability of the 2D Voronoi model to capture the mechanisms leading to size effects in real foams is critically addressed. Finally, Section 5 underlines the most important conclusions of this study.

2. Numerical methods

2.1. Voronoi tessellations

In order to mimic the mechanical behavior of cellular solids, 2D Voronoi tessellations (see e.g. Fig. 1) are used. The Voronoi tessellation technique is akin to the foaming process, where bubbles nucleate at random sites and expand in the liquid material: if all cells nucleate at the same time, grow with the same linear growth rate in all directions while all nuclei remain fixed at the initial location, and the growth ceases for each cell as soon as it touches a neighboring cell, the final space-filling packing of cells is identical to a Voronoi tessellation (see e.g. Zhu et al. [33] and references therein). Of course a foaming process is much more complicated than the idealized model described here; yet, the experimentally measured topological parameters (such as the average number of struts per cell face and the average number of faces per cell) of many foams are in close agreement with the corresponding values for Voronoi tessellations (see e.g. Gibson and Ashby [34], Andrews and Gibson [35]). Based on the assumptions above, the final shape and size of the cells are uniquely determined by the initial distribution of the nuclei. For a regular hexagonal packing with n nucleation points (i.e. n cells) in an area A, the distance between any two adjacent nuclei, r, is equal to

$$r = \sqrt{\frac{2A}{\sqrt{3}n}}. \tag{1}$$

If these n nucleation points are randomly placed in the area A, while the distance between any two nuclei is kept larger than a minimum allowable distance, s, the so-formed diagram is called a δ-Voronoi tessellation, with a randomness level of $\delta = s/r$ (see e.g. Zhu et al. [36] and references therein). The measure of randomness ranges from $\delta = 1$ to $\delta = 0$, respectively, corresponding to the regular case of perfect hexagons, and to the fully random case that is often referred to as the Γ-Voronoi tessellation. Here, δ-Voronoi microstructures with a randomness level of $\delta = 0.7$ are used.

Due to the fact that 2D Voronoi microstructures, similar to real 3D metal foams, have isotropic overall mechanical properties, and deform primarily by cell wall bending, they are often used as a model material. However, unlike real metal foams, Voronoi microstructures still have a relatively elongated yield surface in the $\sigma_1 = \sigma_2$ direction, owing to their high hydrostatic to compressive strength ratio. Numerical studies have shown that displacing the triple junctions where cell walls meet decreases the hydrostatic strength of Voronoi microstructures (as observed for perfect hexagonal microstructures in Chen et al. [37]), leading to the more circular yield surface of real metal foams (for the yield surfaces of metal foams, see e.g. Gioux et al. [38], Deshpande and Fleck [39], Doyoyo and Wierzbicki [40]). Therefore, the junction nodes of the Voronoi diagrams are displaced in a random direction θ, over a random distance b chosen from a uniform distribution $[0, \alpha l_m]$, where l_m is the minimum cell wall length among those connected to that junction, and α is a constant taken to be 0.2. For

[1] Although the experimental results are for metal foams, the tendencies are shared by a large family of foams made of different materials.

more details on the Voronoi microstructures used in this study, the reader is referred to Tekoğlu [41] and references therein.

2.2. Finite element calculations

The finite element calculations are performed by using the commercial software ABAQUS. Cell walls are modeled as elasto-plastic, quadratic Timoshenko beam elements (B22 element of the ABAQUS element library) with a Young's modulus of $E = 70$ GPa, a Poisson ratio of $\nu = 0.33$, and an initial yield stress of $\sigma_0 = 130$ MPa. It is assumed that all the cell walls in a microstructure have the same thickness t. For 2D microstructures, the relative density ρ reduces to the area fraction of the solid cell wall material, which is directly proportional to the cell wall thickness t and given as

$$\rho = \frac{t\sum_{i=1}^{k} l_i}{A}, \tag{2}$$

where A is the area of the microstructure, l_i is the length of cell wall i, and k is the total number of cell walls in A. The relative density of all microstructures is chosen to be $\rho = 0.1$, which is large enough to avoid premature elastic buckling of cell walls. Stocky cell walls with a thickness to length ratio t/l_i larger than 1/2, which cannot be modeled as beam elements, are removed from the microstructures. After the removal process, the cell wall thickness is rearranged to have $\rho = 0.1$; there still remains some stocky cell walls in the structure, with $t/l_i > 1/3$, they make up only a couple of percent of the cell walls. The length of the Timoshenko beam elements are taken to be equal to t, in which case the number of elements used to model a cell wall becomes l_i/t. For relatively long cell walls, l_i/t can reach 30–40, which excessively increases the computational time. Therefore, the maximum number of beam elements used to model a cell wall is limited to 15, which is shown to give a converged solution for different loading conditions. In order to avoid numerical problems commonly encountered in perfect plasticity, linear isotropic strain hardening with a slope $d\sigma/d\varepsilon = 735$ MPa is employed, which was found to have no effect on the effective mechanical properties of the samples normalized by the corresponding bulk values (see Section 3.1).

2.3. Strain mapping

In order to be able to evaluate the deformation and strain localization mechanisms for the Voronoi diagrams, a strain mapping procedure is developed. Each cell (thick black lines in Fig. 2) is divided into triangles (thin red lines in Fig. 2) by using the Delaunay triangulation technique. Note that cells are triangulated individually, using only the vertices of a single cell for the triangulation; that is, the Voronoi diagram and the Delaunay triangulation shown in Fig. 2 are not dual graphs of each other. The displacements of cell vertices, which correspond to the vertices of the triangles as well, are obtained by the finite element calculations. The strains ($\varepsilon_{ij} = 1/2(u_{i,j} + u_{j,i})$, $i, j = 1, 2$) and rotation about the x_3 axis

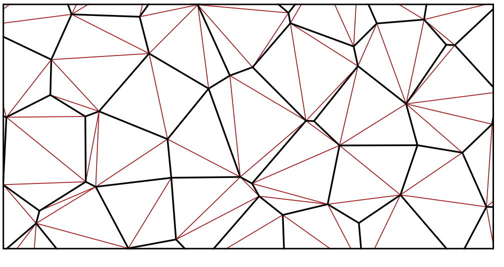

Fig. 2. Delaunay triangulation of the Voronoi diagrams. Cells (thick black lines) are triangulated individually, using only the vertices of a single cell for the triangulation; the Voronoi diagram and the Delaunay triangulation (thin red lines) are not dual graphs of each other. Stocky cell walls with a thickness to length ratio t/l_i larger than 1/2 are removed, and the junction nodes are displaced in a random direction θ, over a random distance b chosen from a uniform distribution $[0, 0.2l_m]$, where l_m is the minimum cell wall length among those connected to that junction.

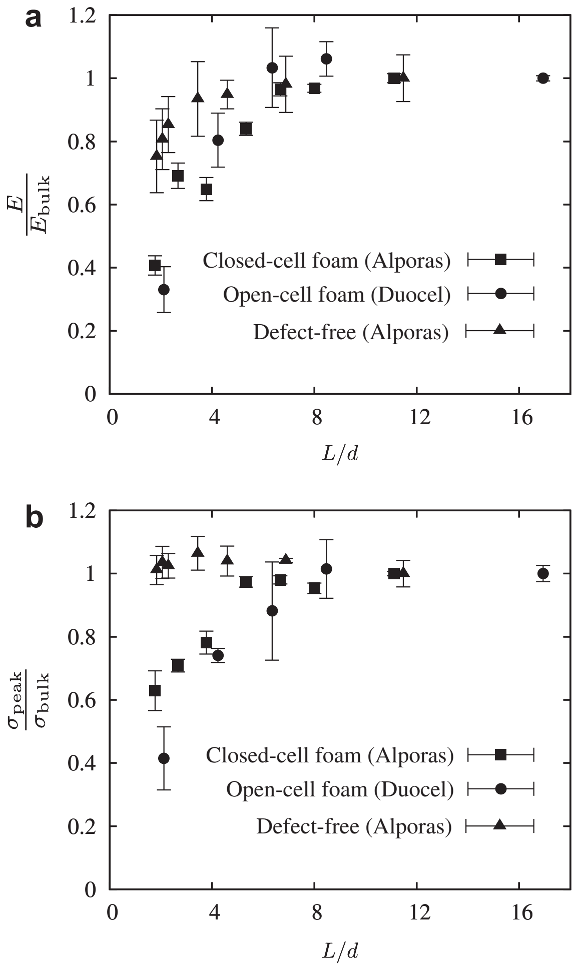

Fig. 3. Experimental results for the open- and closed-cell aluminum foams: (a) normalized unloading Young's modulus, E/E_{bulk} and (b) normalized plastic collapse strength (peak stress), $\sigma_{peak}/\sigma_{bulk}$, plotted against specimen edge length, L, normalized by the cell size, d. The results for the defect-free Alporas foams are taken from Jeon and Asahina [12], and for other foams from Andrews et al. [11].

($w_{12} = 1/2(u_{2,1}-u_{1,2})$) in each triangle are calculated from the nodal displacements using standard finite element techniques. A similar strain mapping procedure is used by Tekoğlu and Onck [42].

3. Results

3.1. Uniaxial compression

A large experimental literature is available on uniaxial compression of metal foams, while only few studies focus on the effect of the sample size under compression; Fig. 3 shows the results of two such studies, Andrews et al. [11] and Jeon and Asahina [12]. In Andrews et al. [11], open-cell aluminum foam (Duocel) cylinders with a height-to-diameter ratio of $H/L = 2$ and a nominal density of $\rho \approx 7\%$, and closed-cell aluminum foam (Alporas) square prisms with a height-to-width ratio of $H/L = 2$ and a nominal density of $\rho \approx 8\%$ are tested. The specimen geometry is kept constant wile changing the

L/d ratio,[2] where d is the average cell size and measured as $d \approx 3$ mm and $d \approx 4.5$ mm for the Duocel and the Alporas foams, respectively. In Jeon and Asahina [12], cubic samples of Alporas foam with different edge lengths, L, are tested, for which the average cell size is measured as $d \approx 4.36$ mm. The data corresponding to Jeon and Asahina [12] represents samples without structural defects-such as partially coupled cells, missing cells, and collapsed cells-which are normally observed in closed-cell aluminum foams. In order to obtain a specimen group without structural defects (which will be referred to as "*defect-free*" in the following) Jeon and Asahina [12] first selected the specimens that fall in a narrow range of relative density, $\rho \approx 8.15$–8.70%, which already excludes specimens containing cells with significant defects. Then, they refined their selection by observing the surface of each specimen with the naked eye as well as with a digital microscopic system. Based on the investigation of each cell on the surface, they estimated cell structures and structural defects inside the specimens, a method they report to be effective especially in the small specimen size regime, i.e. $L/d \lesssim 6$. For specimens with a larger volume, surface observations do obviously not allow an accurate prediction of the inner cell structure. Yet, as also shown in Fig. 3, Jeon and Asahina [12] found that the compressive properties are size-independent for specimens with $L/d > 6$, indicating that the volume fraction of structural defects in these specimens is nearly the same as that of the bulk foam. In both studies, the Young's modulus, E, is taken to be the slope of the unloading curve, and the plastic collapse stress is taken as the initial peak stress σ_{peak}. Bulk material properties, E_{bulk} and σ_{bulk}, are obtained by testing specimens with the largest size (at least $L/d > 5$ in each case). Each data point in Fig. 3 corresponds to the average value of 3–5 specimens for the Duocel foams, 5–9 specimens for the Alporas foams in Andrews et al. [11], and 7 specimens for the defect-free Alporas foams in Jeon and Asahina [12].

Fig. 3a shows the normalized Young's modulus, E/E_{bulk}, as a function of the normalized sample size, L/d. The general trend is the same in all three sets of specimens in the sense that the Young's modulus decreases with decreasing L/d, in the regime where $L/d < 6$ for the Alporas and defect-free Alporas foams, and $L/d < 8$ for the Duocel foams. The Duocel foams have a more pronounced reduction in stiffness compared to the two Alporas sets. The decrease in the Young's modulus of the Alporas foams of Andrews et al. [11] is much more severe compared to that observed in the defect-free Alporas foams of Jeon and Asahina [12]: for a sample size of $L/d \leqslant 2$, E/E_{bulk} given in Andrews et al. [11] is approximately two times less than the corresponding value given in Jeon and Asahina [12]. This large difference between the two Alporas sets cannot be fully attributed to the differences in geometry, density and fabrication methods of the test specimens, nor to the differences in experimental setups; obviously, it partly originates due to the difference in the density of structural defects for the two sets.

Fig. 3b shows the normalized peak stress, $\sigma_{\text{peak}}/\sigma_{\text{bulk}}$, as a function of the normalized sample size, L/d. For the foams of Andrews et al. [11], $\sigma_{\text{peak}}/\sigma_{\text{bulk}}$ follows the same trend as E/E_{bulk} and decreases with decreasing L/d, in the regime of $L/d < 6$ for the Alporas foams, and $L/d < 8$ for the Duocel foams. The defect-free Alporas foams of Jeon and Asahina [12], however, show a size-independent behavior for $\sigma_{\text{peak}}/\sigma_{\text{bulk}}$ in the regime $L/d \geqslant 1.834$. It is worth mentioning that, in terms of size effects, the results of the compression experiments performed on Alporas foams in Bastawros et al. [10]-not shown here-closely agree with those of Jeon and Asahina [12] for E/E_{bulk}, and with those of Andrews et al. [11] for $\sigma_{\text{peak}}/\sigma_{\text{bulk}}$.

Fig. 1a shows the dimensions of a Voronoi sample together with the boundary conditions for uniaxial compression. The samples are compressed in the vertical direction (x_2 axis) while the left and right boundaries are traction free. The set of boundary conditions that can be applied at the top and bottom boundaries is not unique, and it can considerably influence the mechanical response of the samples, see e.g. Chen et al. [37], Alkhader and Vural [43]. Here we apply a vertical displacement u_2^J to all top nodes J according to $u_2^J = \varepsilon_{22} x_2^J$, with x_2^J being the vertical coordinate of the top nodes J. Furthermore, we specify the horizontal force and the rotation of the top nodes to be zero. The same boundary conditions are applied to the bottom nodes J; since x_2^J is zero for the bottom nodes, $u_2^J = 0$ as well. These boundary conditions allow global deformation of the microstructure, avoiding localized deformation near the boundaries. The macroscopic compressive stress is calculated by

[2] In FE calculations, the cell size d is defined as the diameter of a circle whose area is the same as the average area of the Voronoi cells.

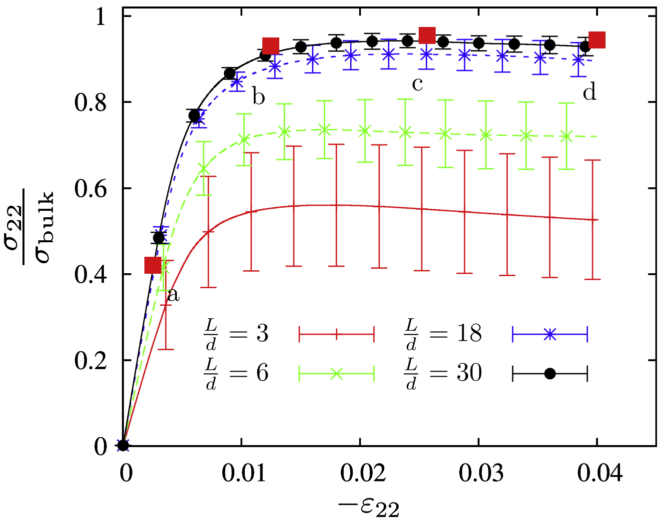

Fig. 4. Stress–strain curves (under compression) for a selection of L/d values. Each curve represents the average stress for 10 different Voronoi realizations.

dividing the sum of the reaction forces at the top nodes by the surface area under compression, Lb, where b is the out-of-plane thickness.

The effect of the sample size on the overall compressive response is investigated using Voronoi microstructures with a constant aspect ratio, $H/L = 2$, but with different lengths under compression, L, similar to the samples used in Andrews et al. [11]. Fig. 4 shows typical stress–strain curves for 2D Voronoi samples for a selection of L/d values. Each curve corresponds to the average response of 10 different Voronoi realizations, plotted together with the standard deviation: the Young's modulus (i.e. the slope of stress–strain curves in the beginning of the elastic regime) and the plastic collapse strength (i.e. the peak stress) increase with increasing sample size, whereas the standard deviation decreases for larger samples. Figs. 5a and b show E/E_{bulk} and $\sigma_{peak}/\sigma_{bulk}$, as a function of L/d, respectively.[3] The results closely agree with the experiments of Andrews et al. [11] in terms of the decreasing stiffness E and plastic collapse strength σ_{peak} with decreasing L/d, the difference being that the reduction rate is somewhat slower for the Voronoi samples. Also, convergence to the bulk values is postponed to slightly larger lengths for the Voronoi model compared to the experimental results for both open- and closed-cell foams. Note that there is an important difference between the dependence of the bulk properties on the relative density in 2D honeycombs and 3D real foams: Young's modulus E_{bulk} varies with relative density cubed for 2D samples, but squared for foams; similarly, strength σ_{bulk} varies with relative density squared for 2D samples, but to the power 1.5 for foams. This difference contributes to the discrepancy between the results for the 2D Voronoi samples and for real foams. As mentioned earlier in the introduction section, to avoid numerical problems encountered in perfect plasticity, a linear isotropic strain hardening with a slope of $d\sigma/d\varepsilon = 735$ MPa is employed to model the cell wall material of the Voronoi samples. Fig. 5b shows the effect of cell wall strain hardening by plotting an additional set of data with a different hardening slope, $d\sigma/d\varepsilon = 335$ MPa (circular symbols), for three different lengths, $L/d = 3,14$, and 30; it is clear that strain hardening has almost no effect on the normalized macroscopic properties.

Keeping the H/L ratio constant does not allow independent analysis of the size effects associated with the height H and the length L of the samples. Therefore, we also tested Voronoi microstructures with a fixed $L/d = 54$, for an increasing H/d, and with a fixed $H/d = 24$, for an increasing L/d. Figs. 6a and

[3] E_{bulk} and σ_{bulk} correspond to the values obtained for the largest Voronoi samples tested in this study, with $L/d = 54$ and $H/d = 24$, as discussed later in this section.

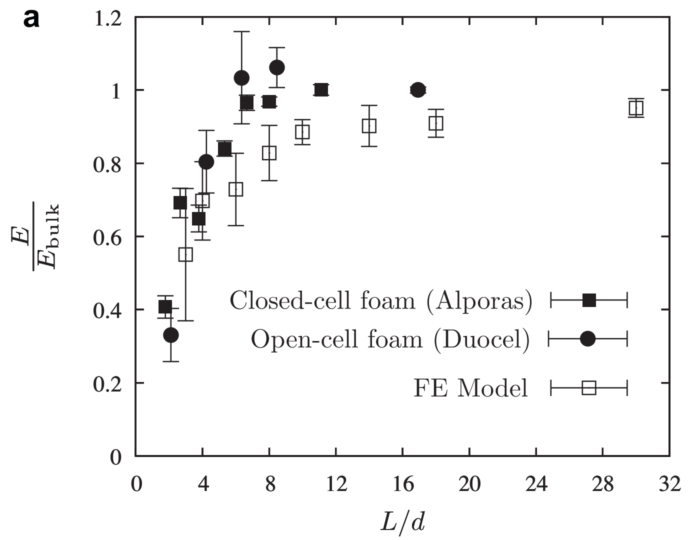

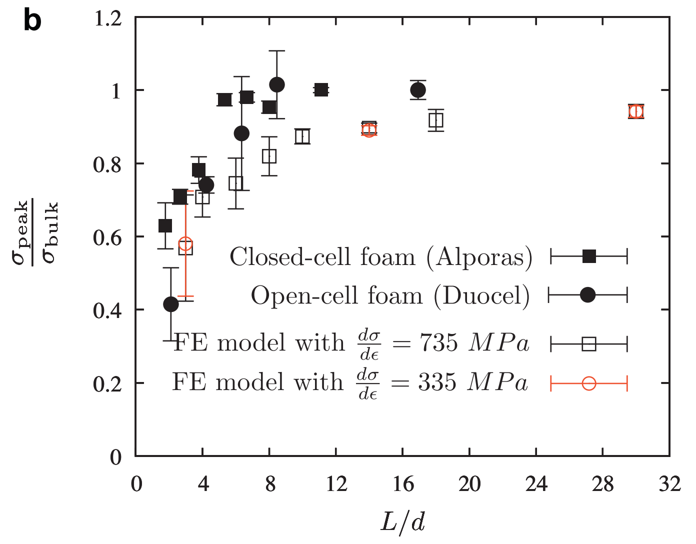

Fig. 5. Comparison of the (2D Voronoi) FE model with experiments (Andrews et al. [11]): (a) normalized Young's modulus, E/E_{bulk}, and (b) normalized plastic collapse strength, $\sigma_{\mathrm{peak}}/\sigma_{\mathrm{bulk}}$, plotted against normalized specimen edge length, L/d.

b show $\sigma_{\mathrm{peak}}/\sigma_{\mathrm{bulk}}$ (square symbols) together with E/E_{bulk} (circular symbols), for samples with a constant L and a constant H, respectively. Note that the horizontal axis values corresponding to the data points for E/E_{bulk} are slightly shifted to the right by adding 1.5, to easily distinguish the two sets of data. Both σ_{peak} and E increase with decreasing H/d, the effect being slightly more pronounced for E (see Fig. 6a. In Chen and Fleck [18], it is also shown that the yield strength of perturbed hexagons increases with decreasing H/d; in contrast, they did not observe any effect of H/d on the yield strength of perfect hexagons). With decreasing L/d, on the other hand, both σ_{peak} and E decrease, where the reduction in the Young's modulus E is greater than that in the peak stress σ_{peak} (see Fig. 6b). In both cases of changing height and changing length, the standard deviation is larger for E than it is for σ_{peak}. Most importantly, the effect of the decreasing length is much larger compared to the effect of the decreasing

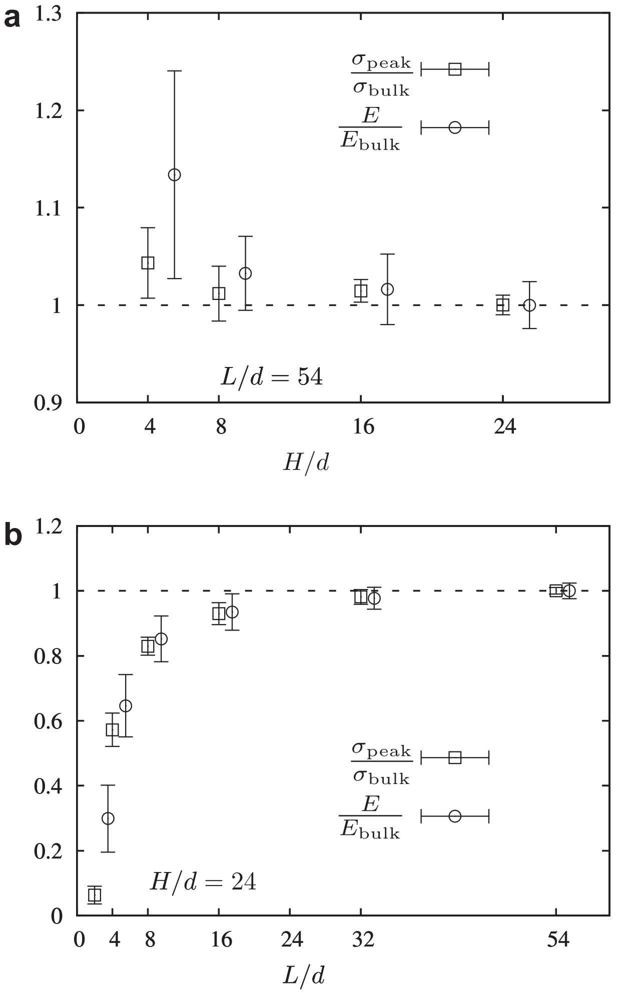

Fig. 6. Normalized effective yield strength ($\sigma_{peak}/\sigma_{bulk}$, square symbols) and stiffness (E/E_{bulk}, circular symbols) of Voronoi microstructures (a) with $L/d = 54$, for increasing H/d, and (b) with $H/d = 24$, for increasing L/d. H/d and L/d for E/E_{bulk} are shifted to the right by 1.5 units, to distinguish the two sets of data points.

height, meaning that the tendencies observed in Fig. 5 are primarily related to the change in L/d (i.e., area under compression). Considering the results presented in Figs. 5 and 6, it is clear that to obtain the bulk compressive mechanical properties of a Voronoi microstructure, a block of dimensions $H/d \geqslant 16$ and $L/d \geqslant 32$ is necessary.

Figs. 7a, c, e, and g show the distribution of $-\varepsilon_{22}$, ε_{11}, ε_{12max}, and $-\omega_{12}$ (=$-(u_{2,1} - u_{1,2})/2$), respectively, throughout a sample with dimensions of $H = 2L = 36d$, at a macroscopic compressive strain value corresponding to point "*b*" in Fig. 4; Figs. 7b, d, f, and h show corresponding values at the point "*d*" on the stress–strain curve of Fig. 4. Note that "*b*" corresponds to a relatively early stage of strain localization in narrow bands, and "*d*" to the final point in strain history. Here, ω_{12} is a component of the classical macroscopic rotation tensor, and it measures the in-plane macroscopic rotation of the Voronoi cells. ε_{12max} is the shear strain plotted with respect to a reference frame obtained by rotating the original reference frame (which is used for ε_{11}, ε_{22} and ω_{12}, and whose axes coincide with the principal

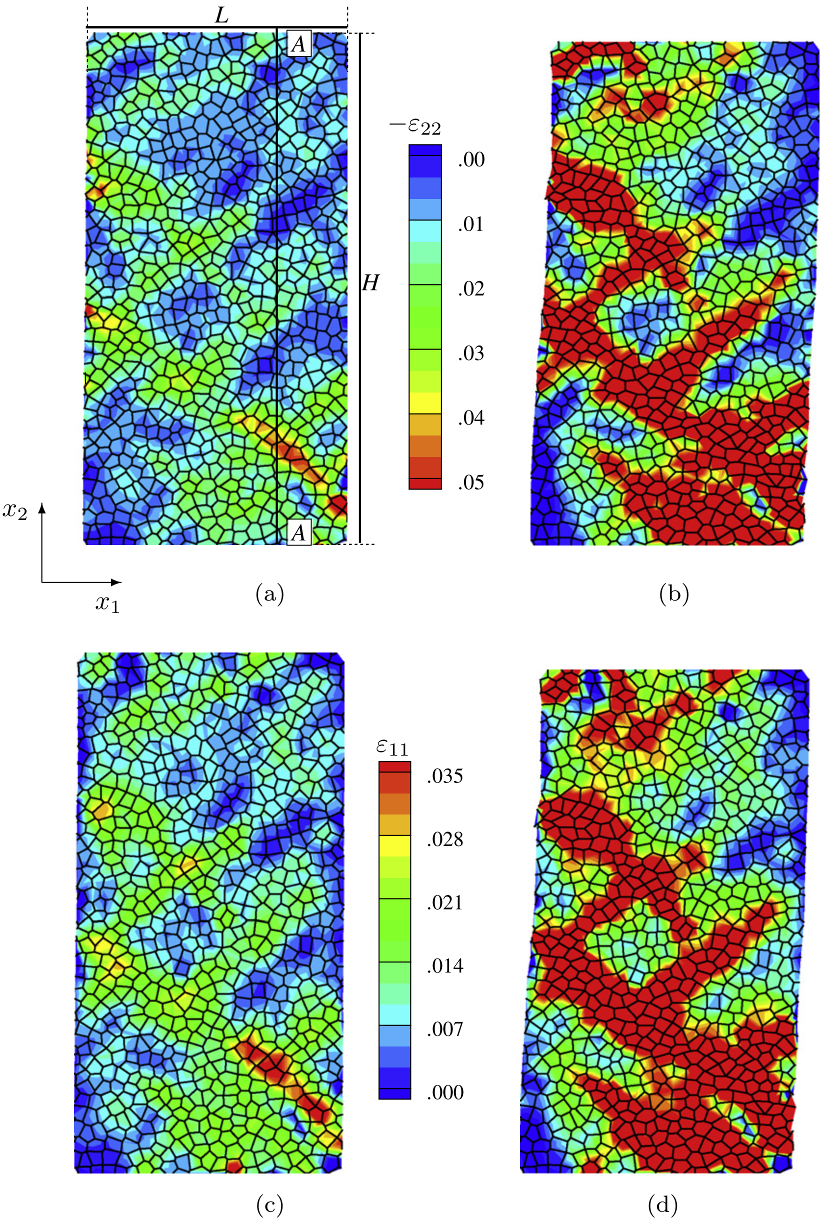

Fig. 7. (a), (c), (e) and (g) show the distribution of $-\varepsilon_{22}$, ε_{11}, ε_{12max} (with respect to a 45° counter-clockwise rotated reference frame) and $-\omega_{12}$, respectively, throughout a sample with dimensions of $H = 2L = 36d$, at a macroscopic strain value corresponding to point "*b*" in Fig. 4. Figures (b), (d), (f) and (h) show $-\varepsilon_{22}$, ε_{11}, ε_{12max} and $-\omega_{12}$ for a larger strain (point "*d*" in Fig. 4).

strain directions) 45° about the x_3 axis in the counter-clockwise direction, and it is expected to give the maximum in-plane shear strain. We see that localized deformation bands with a width of about ~1.5 cell diameters – which were already initiated in the elastic regime – become clearly visible at the macroscopic strain value for point "*b*". These deformation bands are aligned ≈∓45° with respect to the x_2

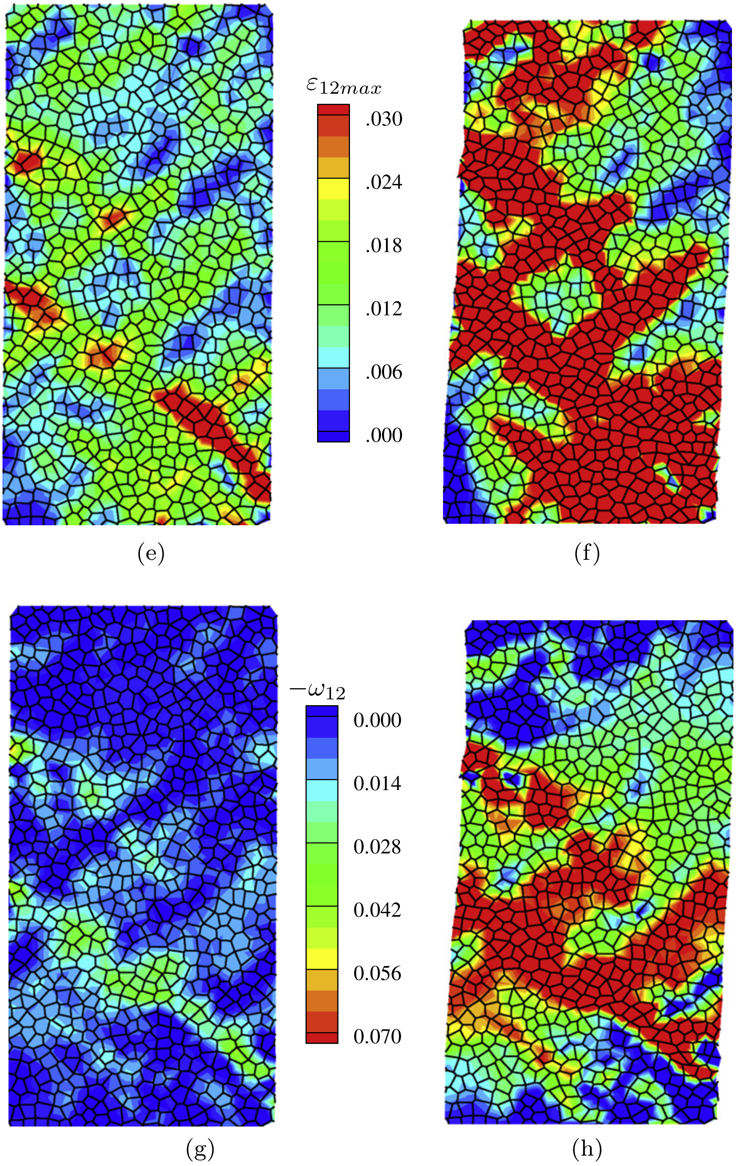

Fig. 7 (*continued*)

axis, that is in the direction of the maximum shear strain. With further deformation, the bands enlarge both in thickness and length as can be seen from the strain maps plotted for point "*d*".

Fig. 8 shows: (a) $-\varepsilon_{22}$ and ε_{11} and (b) ε_{12max} and $-\omega_{12}$, respectively, as a function of the x_2 axis position, normalized by the average cell size, *d*, through the line A–A (see the inset of Fig. 7a). For each variable, 4 curves with different thicknesses are plotted, each curve corresponding to a different macroscopic strain level, denoted as "*a*, *b*, *c*, and *d*" in Fig. 4. In each figure, the curve for the smallest macroscopic compressive strain level ("*a*") has the smallest, and that for the largest strain level ("*d*") has the largest thickness. For the strain level "*a*", all four deformation measures are nearly zero trough the

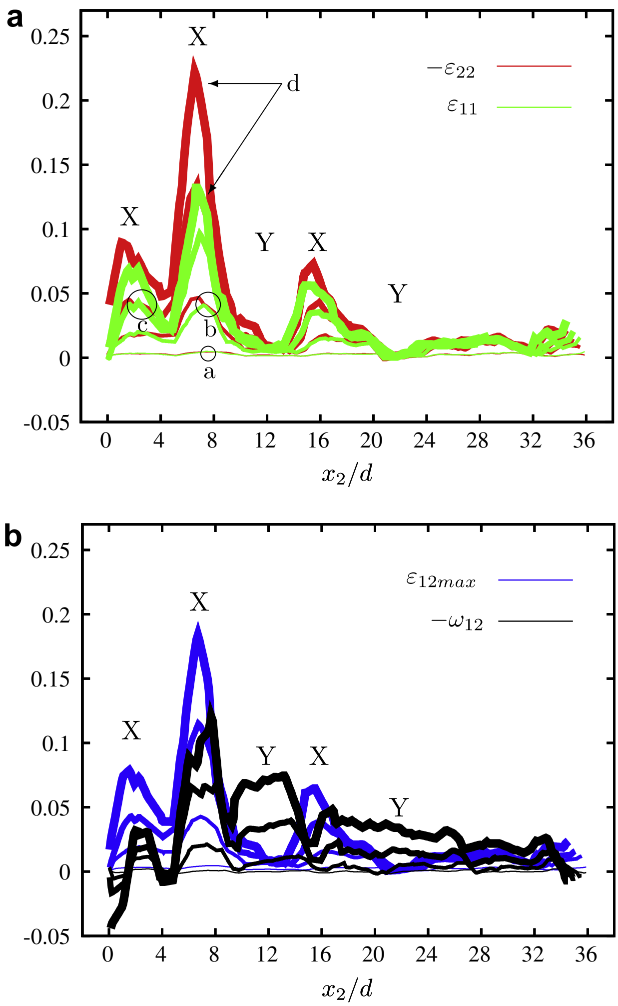

Fig. 8. The variation of (a) $-\varepsilon_{22}$ and ε_{11}, and (b) ε_{12max} (with respect to a 45° counter-clockwise rotated reference frame) and $-\omega_{12}$, as a function of the x_2 axis position through the line A–A (see the inset of Fig. 7a). For each variable, four curves with different thicknesses are plotted, each curve corresponding to a different macroscopic strain level, denoted as "*a*, *b*, *c* and *d*" in Fig. 4. The curve for the smallest strain value (point "*a*") has the smallest, and for the largest strain value (point "*d*") has the largest thickness.

entire line, whereas for level "*b*", deformation starts to localize in the cells located at the positions corresponding to the peaks of the curve. At strain levels "*c* and *d*", the locations of the peak values do not change: once the deformation localizes in a region, further macroscopic compressive strain increases the intensity of the localization in that region, while the neighboring cells are forced to accommodate this localized deformation. We observe mainly two distinct cell deformation mechanisms, designated, respectively, as X and Y in Fig. 8. The mechanism X, for which all of the four deformation measures produce a peak, represents both distortion and rotation of cells; these cells are part of the localized deformation bands. The mechanism Y, on the other hand, involves mainly rigid body rotation of the cells, with minimal distortion and shear measures; these cells are adjacent to the localization bands.

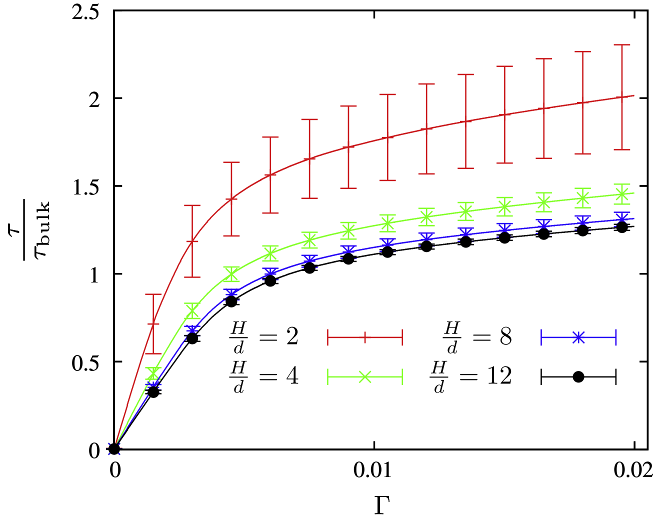

Fig. 9. Stress–strain curves (under shear) for a selection of H/d values. Each curve represents the average stress for 10 different Voronoi realizations.

3.2. Shear

In this section, we study the shear boundary value problem as shown in Fig. 1b. In order to analyze the (deformation) mechanisms that give rise to size effects, the height H of the samples is gradually increased. As in the experimental study of Andrews et al. [11], the aspect ratio of the samples is kept constant at $L/H = 12$, and the boundary conditions correspond to sticking grips (see Fig. 1b). At the nodes of the bottom boundary, all three degrees of freedom of the beam elements are fixed: $u_1^J = u_2^J = \phi^J = 0$. At the top boundary, the degrees of freedom of all the nodes are kinematically coupled to those of a reference node R, which is displaced through $u_1^R = \Gamma H$, while specifying $F_2^R = \phi^R = 0$. In doing so, the top nodes are constrained to remain on a straight horizontal line, while this horizontal line is allowed to displace in the vertical direction to accommodate the shear deformation.

Fig. 9 shows typical stress–strain curves for Voronoi samples with different heights, where each curve represents the average of 10 different realizations. In real foams, the strain hardening regime that starts after the elastic deformation is followed by a drop in the measured stress due to distributed microcracking in cell-walls and/or -faces (see e.g. Andrews et al. [11], Chen and Fleck [18]). For the Voronoi samples, however, the microcracking effect is not accounted for; therefore, the overall stress continuously increases. We see that the stiffness and strength of the samples decrease with increasing height, and the stress–strain curves converge to that of the bulk material for $H/d > 8$. In addition, the standard deviation of the average stress value diminishes with increasing height, being almost zero for $H/d = 12$.

Figs. 10a and b show the effect of the specimen height on the shear stiffness, G, and the shear strength, τ_0, of the Voronoi samples, respectively. The shear stiffness G is obtained from the slope of the stress–strain curves in the elastic regime, and the shear strength τ_0 is defined as the stress value corresponding to an offset strain of 0.2%. We see that both the stiffness and the strength of the Voronoi samples, as well as their standard deviation, increase with decreasing sample height: a size effect opposite to that observed under uniaxial compression. The size effect, being more pronounced for G compared to τ_0, vanishes for samples with $H/d \geqslant 8$. In Fig. 10b, the normalized shear strength ($\tau_0/\tau_{\text{bulk}}$) of closed-cell aluminum (Alporas) foams obtained by Andrews et al. [11] is also shown, in comparison with the FE results. Similar experimental results have also been obtained by Chen and Fleck [18]. The two individual experimental data points for $H/d \approx 1.3$ correspond to a density of 189 kg/m^3 and 210 kg/m^3, for the lower and the higher shear strength, respectively. Each of the other

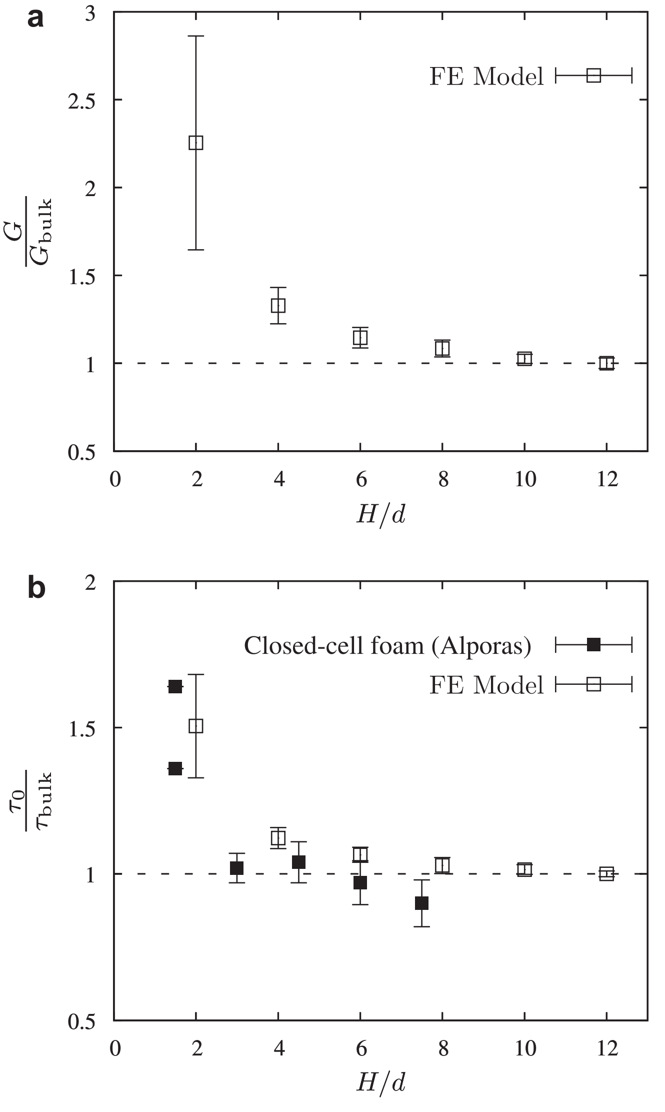

Fig. 10. (a) Shear modulus and (b) shear strength, normalized by the bulk value, plotted against H/d. The experimental results of Andrews et al. [11] for closed-cell aluminum (Alporas) foams are also shown in (b).

experimental data points (for $H/d > 2$) represents the average value for three different specimens, with densities around 200 kg/m^3. The shear strength of the Alporas foams also increases with decreasing height, but the Voronoi model predicts a larger strengthening in the small H/d regime. The bulk value of the shear strength is reached at $H/d \approx 2.7$ and at $H/d \approx 8$, for the Alporas foams and for the Voronoi samples, respectively.[4]

Fig. 11 shows the distribution of $-\varepsilon_{12}$ and ω_{12} for a sample with a height of $H/d = 12$, at two different overall strain levels, $\Gamma = 0.0004$, corresponding approximately to the onset of strain localization,

[4] For the Alporas foams, the fluctuation in the τ_0/τ_{bulk} value for $H/d > 2.7$ is attributed to the slight differences in the density of the specimens, see Andrews et al. [11].

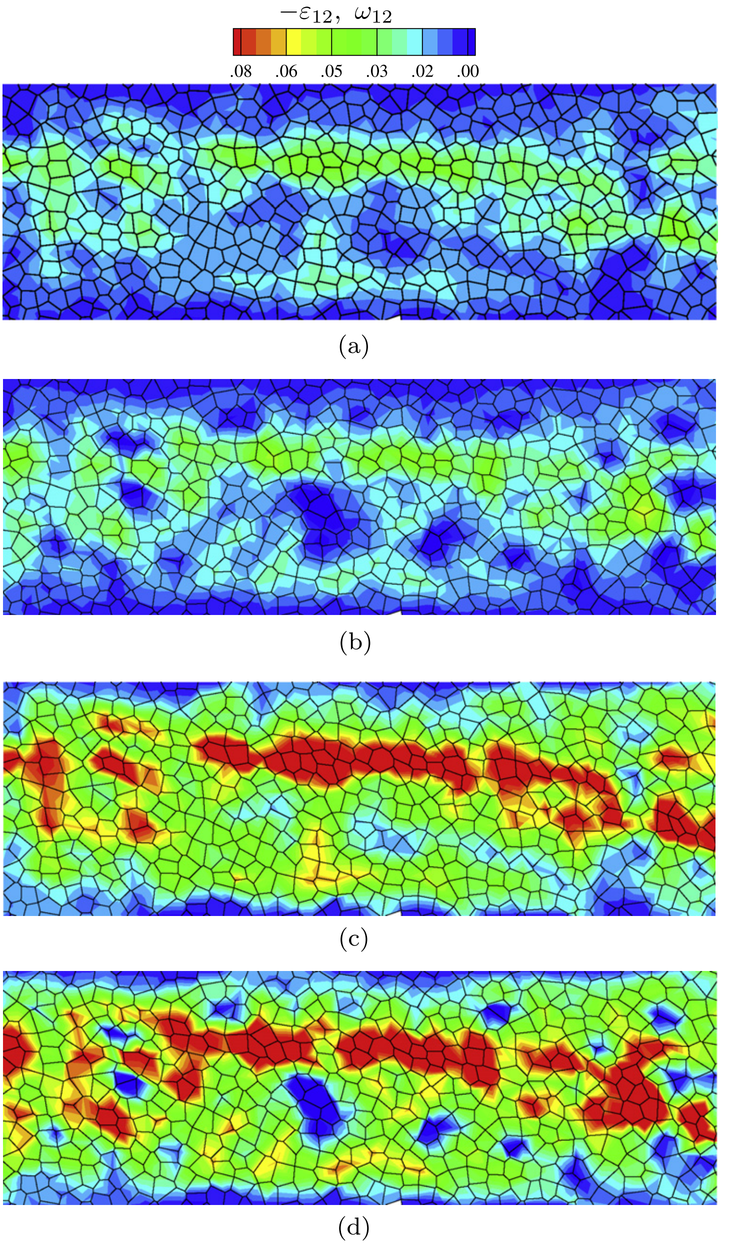

Fig. 11. Shear strain $-\varepsilon_{12}$, (a) and (c), and rotation ω_{12}, (b) and (d), maps for a Voronoi microstructure with $L/H = H/d = 12$, at a relatively low (a and b) and relatively large (c and d) overall strain values, $\Gamma = 0.0004$, corresponding approximately to the onset of strain localization, and $\Gamma = 0.02$ (see Fig. 9), respectively.

and $\Gamma = 0.02$ (see Fig. 9). For both macroscopic strain levels, the shear strain $-\varepsilon_{12}$, as well as the macroscopic rotation ω_{12}, is minimum near the top and bottom boundaries, where the rotation of the cell-walls is fully restricted. These low rotational boundary layers extend over ~1–2 cells from each side. Moving towards the middle of the sample, both $-\varepsilon_{12}$ and ω_{12} gradually increase, reaching a peak

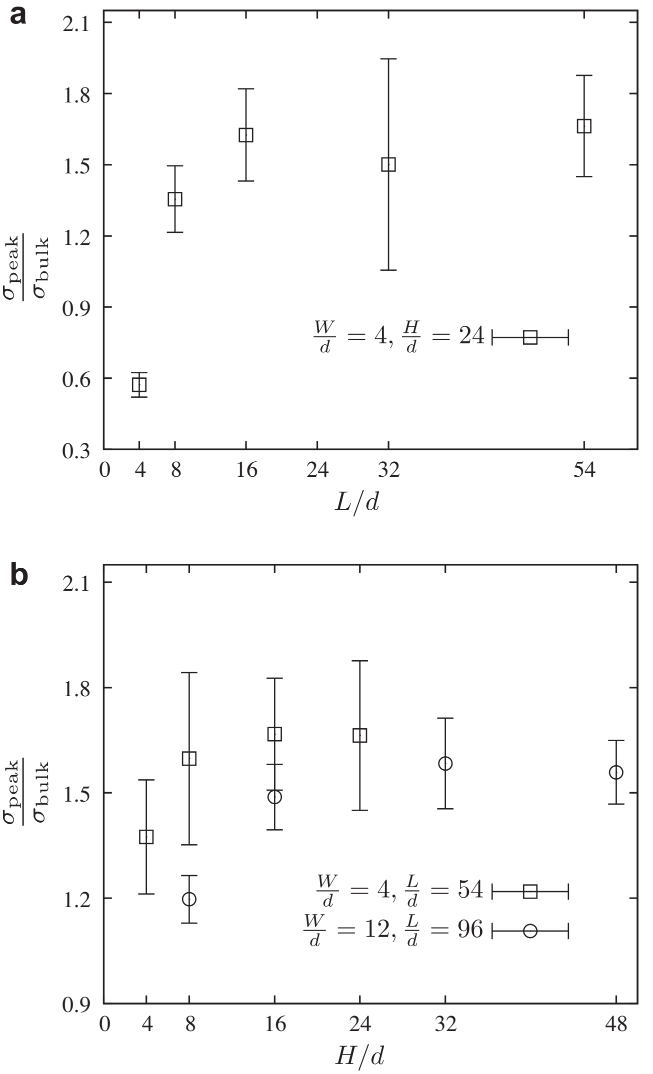

Fig. 12. Convergence study in terms of the indentation peak stress σ_{peak} of the Voronoi samples with: (a) $H/d = 24$, for increasing L/d; (b) $L/d = 54$, square symbols, and $L/d = 96$, circular symbols, for increasing H/d. The indenter size is $W/d = 4$ for (a) $H/d = 24$ and (b) $L/d = 54$ (square symbols), and $W/d = 12$ for (b) $L/d = 96$ (circular symbols).

around $x_2 = H/2$, where the strain localizes in a shear band. Careful observations show that shear and rotation are correlated within the shear bands, whereas they are anti-correlated in the neighboring regions, just outside the shear bands (compare Figs. 11c and d). The FE calculations performed on perfect (see Chen and Fleck [18], Onck et al. [44]) and perturbed hexagons (see Chen and Fleck [18], Diebels and Steeb [45]) closely agree with the results presented here.

3.3. Indentation

The schematic in Fig. 1c shows the dimensions of the indenter and Voronoi samples. Rectangular Voronoi samples of length L and thickness H are vertically indented with a flat-end punch (FEP) of

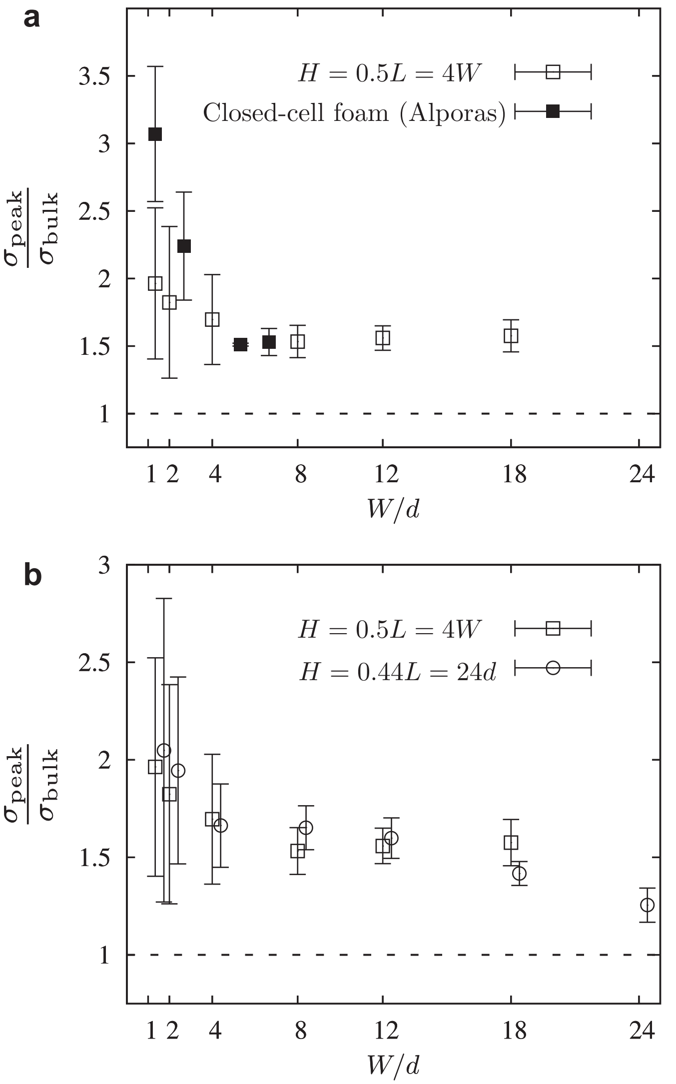

Fig. 13. Indentation peak stress, σ_{peak}, normalized by the uniaxial compression strength, σ_{bulk}, as a function of the indenter width, W/d, for (a) $H = 0.5L = 4W$ (empty square symbols) and experimental results for closed-cell Alporas foams (Andrews et al. [11], filled square symbols), and (b) $H = 0.5L = 4W$ and $H = 0.44L = 24d$ (empty square and circular symbols, respectively). Note that the data points for $H = 0.44L = 24d$ are shifted to the right by adding a value of 0.5 to their W/d values.

width W. The indenter is located at an equal distance from the two free-edges (i.e., left and right boundaries) of the samples. The boundary conditions for the nodes under the indenter and at the bottom boundary are the same as for the uniaxial compression test (see Section 3.1); all other edges are stress free. All three dimensions, L/d, H/d, and W/d, affect the response of the samples. The first two, L/d and H/d, are responsible for edge-effects, and W/d for size effects inherent to the cellular morphology. Experiments show that if L/d is not large enough (i.e., the distance between the indenter and a free-edge is less than ~1 or 2 W/d) cells surrounding the indenter turn to be more compliant compared to the cells located in the bulk, which considerably reduces the resistance to the penetration of the indenter (e.g. Mohan et al. [27], Olurin et al. [29]). If, on the other hand, H/d is

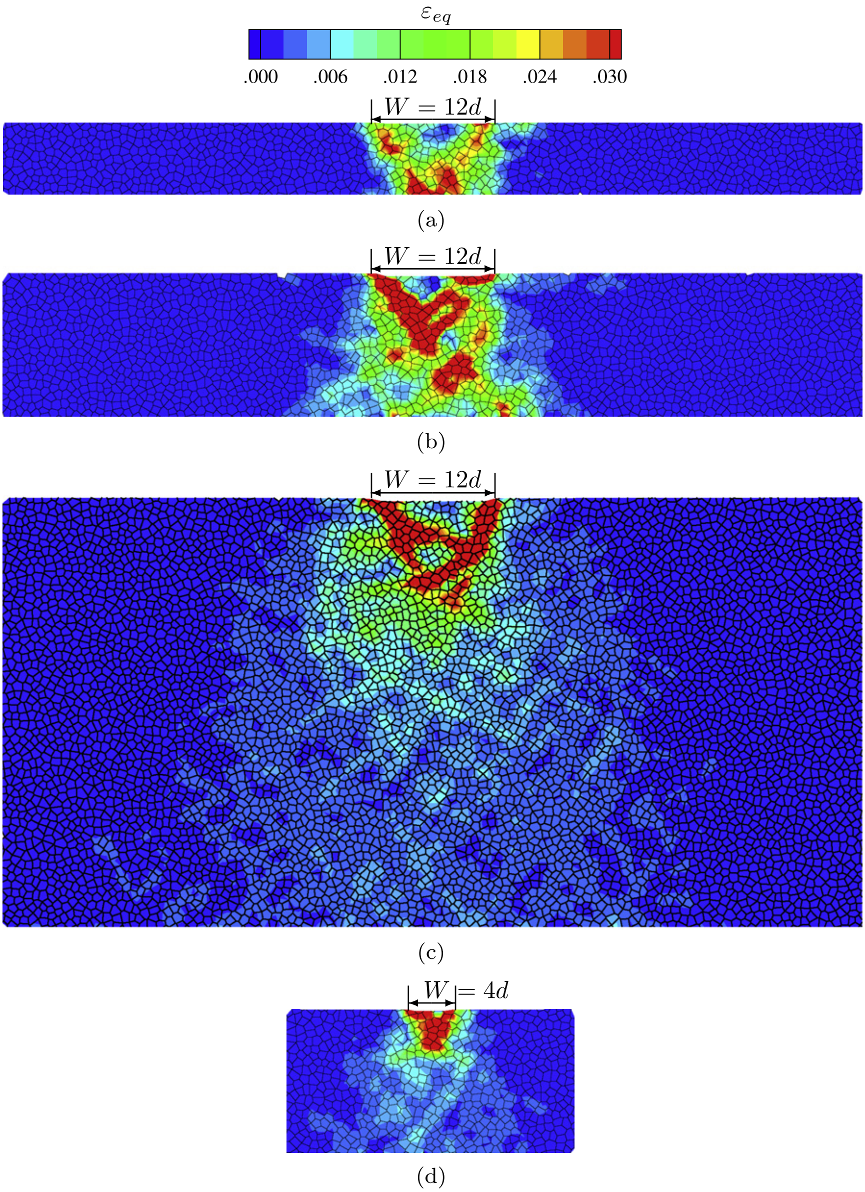

Fig. 14. The equivalent strain (ε_{eq}) distribution for four different samples with (a) $1.5H = 0.125L = W = 12d$, (b) $0.75H = 0.125L = W = 12d$, (c) $0.25H = 0.125L = W = 12d$, and (d) $0.25H = 0.125L = W = 4d$. Each strain map corresponds to a state encountered immediately after the maximum force under the indenter is reached.

not large enough (i.e., the distance between the indenter and the bottom boundary is less than $\sim 2\ W/d$), the bottom boundary will interact with the indenter, which will affect the indentation strength. In order to elucidate the edge-effects on the indentation response of Voronoi samples, a convergence test is performed. Fig. 12 shows the average peak stress σ_{peak} (normalized with σ_{bulk}) of 10 different Voronoi samples as a function of: (a) L/d, for a fixed sample thickness of $H/d = 24$, (b) H/d, for a fixed sample length of $L/d = 54$, square symbols, and $L/d = 96$, circular symbols. The indenter size is $W/d = 4$ for samples with $H/d = 24$ and $L/d = 54$, and $W/d = 12$ for samples with $L/d = 96$. Similar to the results obtained for the compression test, σ_{peak} increases with increasing L/d (compare Figs. 6b and 12a), and a converged value is reached for $L \geqslant 16d$. σ_{peak} increases with increasing H/d as well,[5] but the effect is less pronounced for H/d compared to L/d. Convergence is obtained for approximately $H \geqslant 16d$. Note that, in compression, σ_{peak} follows an opposite trend, and decreases with increasing H/d (compare Figs. 6a and 12b), as it is also the case for indentation experiments (e.g. Kumar et al. [23]); the origin of this difference is further explored in Section 4. The convergence study shows that for an indenter size $W = 4d$ the results are independent of sample dimensions when $L \geqslant 16d$ and $H \geqslant 16d$. This suggests that edge-effects do not influence the results when both L and H are larger than four times the indenter size W. As an additional check, we repeated the convergence test for samples with $L = 2H$, while increasing the ratio L/W for a fixed indenter size $W = 4d$; the same conclusion was reached.

Fig. 13a shows the comparison of σ_{peak} normalized by σ_{bulk} – uniaxial compressive strength – as a function of W/d for Voronoi samples with $H = 0.5L = 4W$ (the sample size is arranged according to the indenter size to avoid edge-effects, empty square symbols), and for experimental results for closed-cell Alporas foams (Andrews et al. [11], filled square symbols, which closely agree with the experiments performed by Olurin et al. [29]). For both the Alporas and the Voronoi samples, σ_{peak}-which is initially (i.e., for $W/d \approx 1, 2$) $\sim$2 or 3 times σ_{bulk}-decreases with increasing indenter size, but for the Alporas foams the size effect is larger in the small W/d regime, and σ_{peak} decreases faster with increasing W/d. For both the experimental and modeling results the scatter increases with decreasing sample size, leading to a reduction in statistical significance for the modeling data. The indentation peak stress converges to $\approx 1.5\sigma_{\mathrm{bulk}}$ for the Alporas foams, and to $\approx 1.65\ \sigma_{\mathrm{bulk}}$ for the Voronoi samples. Onck et al. [44] and Onck [46] performed indentation calculations on perfect and perturbed hexagons, respectively, using the same boundary conditions as given here. In both studies, the dimensions of the samples are kept constant as $H \approx 0.44L \approx 24d$, while increasing the indenter size. We repeated these calculations for Voronoi microstructures, using the same sample dimensions. Fig. 13b compares the results for $H = 0.5L = 4W$ and $H = 0.44L = 24d$ (empty square and circular symbols, respectively). The data points for $H = 0.44L = 24d$ are shifted to the right by adding a value of 0.5 to their W/d values. It is clear that for $W/d \leqslant 12$ the specimen geometry has a marginal effect on the results. For $W/d > 12$, σ_{peak} continues to decrease for samples with $H = 0.44L = 24d$, whereas, as stated earlier, it converges to $\approx 1.65\ \sigma_{\mathrm{bulk}}$ for samples with $H = 0.5L = 4W$. For $H = 0.44L = 24d$, with increasing indenter size, the distance between the indenter and the free-edges of the sample decreases. After $W/d > 12$, the edge-effects start to play an important role, and cause a decrease in σ_{peak}, as also pointed out by the convergence study (see Fig. 12).

Fig. 14 plots the equivalent strain ($\varepsilon_{eq} = \sqrt{2/3\varepsilon_{ij}\varepsilon_{ij}}, i,j = 1,2$) distribution for four different samples with (a) $1.5H = 0.125L = W = 12d$, (b) $0.75H = 0.125L = W = 12d$, (c) $0.25H = 0.125L = W = 12d$, and (d) $0.25H = 0.125L = W = 4d$; i.e. for (a), (b), and (c) the sample length is kept the same, $L = 96d$, while the sample thickness is increased, and for (c) and (d) the ratio of the indenter size to the sample dimensions is kept the same while the indenter size is decreased, $W/d = 12$ and 4, respectively. The strain distribution corresponds to a state after the peak load was reached. In each case, there are two main localized deformation bands which extend from the two edges of the indenter towards the bulk of the material, and the deformation is mainly confined to the zone just beneath the indenter. Similar to compression, the localization bands are aligned in the direction of the maximum shear strain, i.e. $\mp 45^{\circ}$ with respect to the indentation direction for all cases. As can be seen from Figs. 14a–c, at the peak load the deformation has spread to a depth approximately equal to the indenter width. For $H/d = 8$ (Fig. 14a) this results in an interaction with the substrate leading to an earlier onset of localization and an associated lower indentation strength (see Fig. 12b). Comparing the strain maps in (c) and (d) shows that the main difference for the two indenter sizes is the absolute size of the localized deformation area right under the indenter, being smaller for (d) $W/d = 4$.

[5] In Fig. 12b, σ_{peak} is larger for $W/d = 4$ than it is for $W/d = 12$ due to the indenter size effect, which will be explored further in this section.

3.4. Bending

The aim in this section is to understand the deformation mechanisms and associated size effects in the bending of a foam. A bending state for 2D Voronoi samples can be achieved by fixing one end of the samples (with height H and length L) while applying a macroscopic rotation at the other end (see Fig. 1d). In the case of elastic deformation, the macroscopic rotation can be applied through a linearly varying displacement field over the sample height, u_1^J $(x_1 = L) = -cLx_2$. The beam with length L is aligned in the x_1 direction, and x_2 is measured from the midsection of the sample, with c being the curvature of the beam (see also Tekoğlu [41], Tekoğlu and Onck [42]). According to these boundary conditions, u_1^J $(x_1 = L) = 0$ at $x_2 = 0$, i.e., at the neutral axis. Such a restriction in the u_1 displacement of the beam is a valid assumption in the case of small elastic deformations, where the additional normal forces associated with this restriction are negligible compared to the bending moment. In the case of plasticity, however, the contribution from these normal forces – which is proportional to the macroscopic rotation of the beam – considerably affects the sample response. Therefore, in this study, the macroscopic rotation is applied through the rotation of a reference node on a rigid bar that is attached to the end of the samples (see Fig. 1); the macroscopic rotation θ and the reaction moment M of the samples are exactly equal to those of the reference node, which are directly given by the FE calculations at each strain increment. In this arrangement, the samples are allowed to freely move in the x_1 and x_2 directions during bending. The aspect ratio of the samples are kept constant at $L/H = 10$, while gradually increasing the height H. A large aspect ratio avoids possible edge-effects.

Fig. 15 shows the average bending moment – per unit out of plane thickness – M of 10 different Voronoi realizations as a function of the applied macroscopic rotation θ, for different H/d values. We see that the value of the standard deviation is negligible compared to the value of the average bending moment. For each H/d, M initially (i.e., in the small θ regime) increases linearly with increasing θ. This is followed by a nonlinear transition regime after which M continues to increase almost linearly, but with a lower rate than in the initial regime. The nonlinear transition regime corresponds to the formation of a localized plastic hinge, after which the bending moment continues to increase. This point will be discussed later in this section. For the same θ, the value of M as well as its rate of increase is larger for a larger H/d. The bending moment in pure bending is equal to $M = EIc$, where E is the Young's modulus, I is the second moment of area, and c is the curvature of the beam, respectively. For a rectangular cross-section with an out-of-plane thickness b, the second moment of area is given as $I = (bH^3)/12$. Even if the samples were modeled as dense solids instead of Voronoi microstructures,

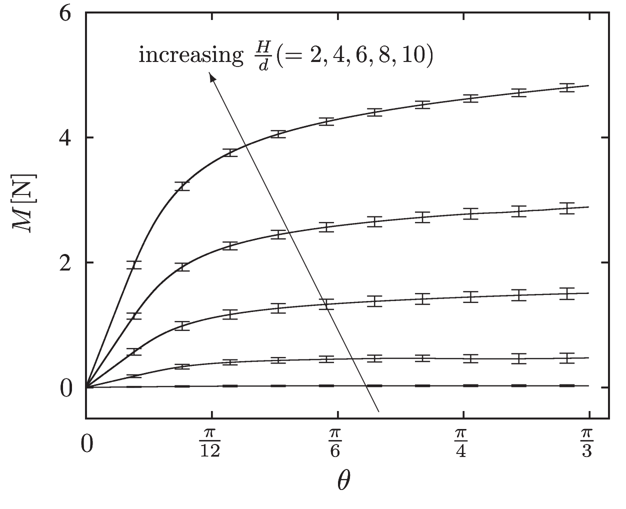

Fig. 15. Bending moment – per unit out-of-plane thickness – M as a function of the applied macroscopic rotation θ for a selection of H/d values. Each curve represents the average of 10 different Voronoi realizations.

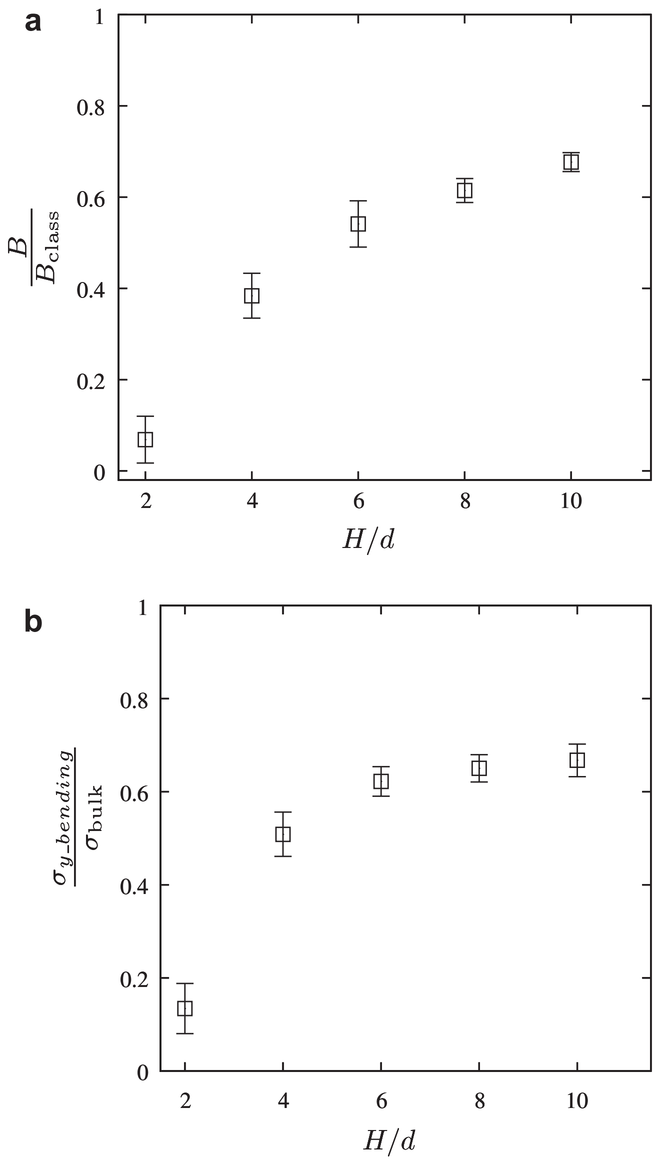

Fig. 16. (a) The normalized macroscopic stiffness B/B_{class}, and (b) the yield strength obtained from bending test $\sigma_{y\_bending}\left(=\frac{6M_{onl}}{bH^2}\right)$, normalized by the uniaxial compression strength, σ_{bulk}, plotted as a function of H/d.

the samples with a larger H would naturally have a larger bending stiffness, EI, and a larger M for the same value of θ. Therefore, in Fig. 15, size effects inherent to the cellular topology of the Voronoi samples are masked by the effect of the cross-section size on bending mechanical properties, which should somehow be excluded from the results. This has been done in Figs. 16a and b, for the elastic and plastic behaviors, respectively. Fig. 16a shows the normalized effective macroscopic bending stiffness B/B_{class} as a function of H/d, with $B = M_iL/\theta_i$ and B_{class} ($=E_{\mathrm{bulk}}bH^3/12$) the classical bending stiffness of a dense sample with the same geometry, dimensions (b,H) and Young's modulus (E_{bulk}) as the Voronoi samples under consideration. Note that M_i is the value of the bending moment corresponding to a very

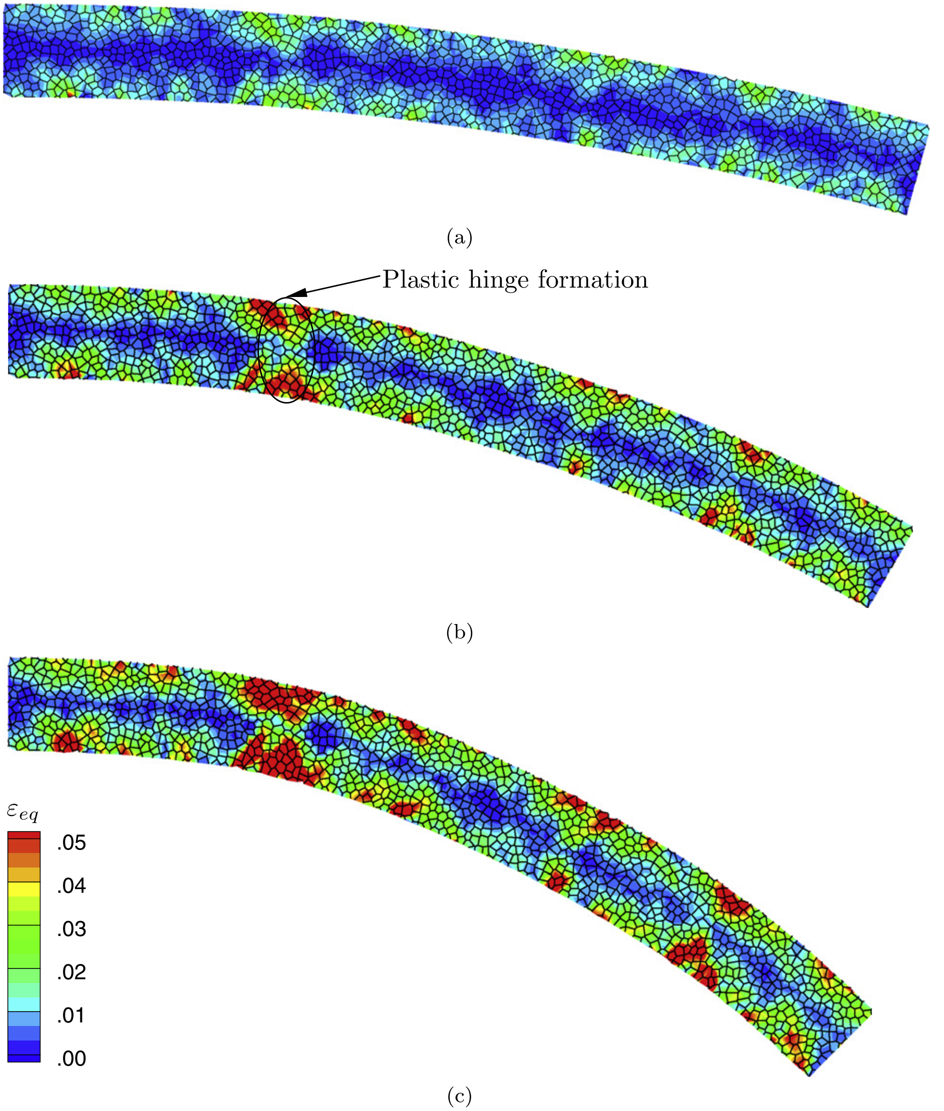

Fig. 17. The equivalent strain ε_{eq} distribution for a sample with H/d = 10, at an applied rotation of (a) $\theta = \frac{\pi}{12}$, (b) $\theta = \frac{\pi}{6}$, and (c) $\theta = \frac{\pi}{4}$.

small macroscopic rotation θ_i, for which the deformation of the sample is fully elastic. The bending stiffness, similar to the compressive stiffness, decreases with decreasing H/d, with the reduction being more pronounced in the case of bending (compare Figs. 16a and 5b). In the small H/d regime $B/B_{class} \ll 1$, and with increasing H/d it tends to converge to 1, although the convergence rate is rather slow. Fig. 16b plots the yield strength obtained from the bending test, $\sigma_{y\_bending}$(=$6M_{onl}/bH^2$), normalized by the bulk compressive strength,[6] σ_{bulk}, as a function of H/d. In the expression $\sigma_{y\_bending} = 6M_{onl}/bH^2$, M_{onl} is the bending moment which corresponds to the onset of nonlinearity, and for the Voronoi diagrams it is defined to be the bending moment M corresponding to an offset rotation of θ = 0.002. In

[6] Note that E_{bulk} and σ_{bulk} are the bulk stiffness and strength values obtained for the Voronoi samples in Section 3.1, see Fig. 6.

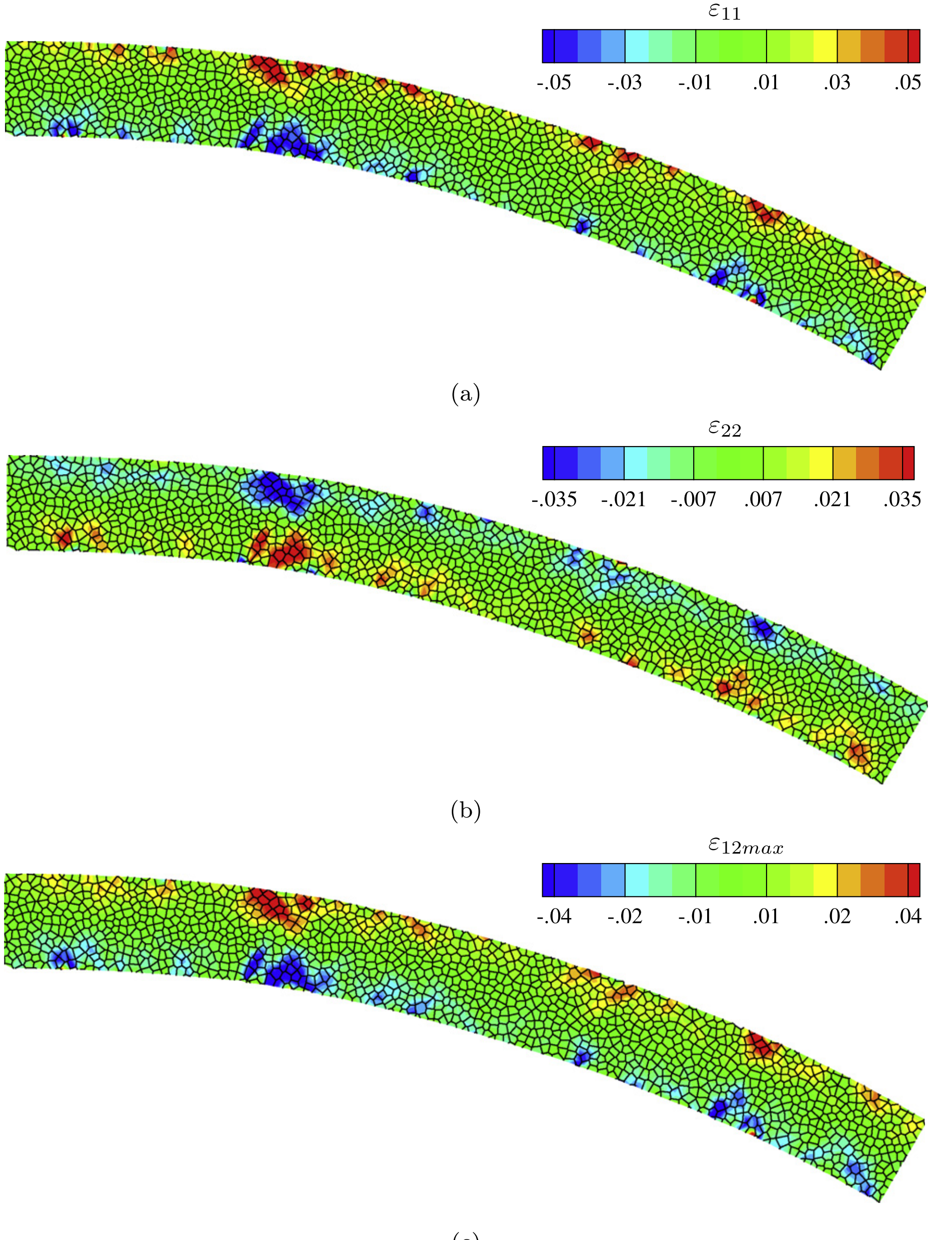

Fig. 18. (a) ε_{11}, (b) ε_{22}, and (c) ε_{12max} distribution for the same Voronoi sample shown in Fig. 17, for $\theta = \frac{\pi}{6}$. ε_{12max} is the shear strain plotted with respect to a 45° counter-clockwise rotated reference frame.

case of an elastic–perfectly plastic material, in the elastic deformation regime the normal stress is linearly distributed through the beam thickness, being zero at the neutral axis. With increasing macroscopic rotation, the stress increases and reaches the yield stress value, σ_{bulk}, initially only at the two surfaces of the beam parallel to the neutral axis; the corresponding bending moment is M_{onl}. Since there is no stain hardening, once the value σ_{bulk} is reached, the stress remains constant with further macroscopic rotation, while the regions of constant stress at the outer fibers of the beam penetrate towards the neutral axis. Finally, plasticity pervades the entire section and a plastic hinge is formed (see e.g. Fig. 17). As discussed earlier in Sections 2.2 and 3.1, here we employed linear strain hardening for the cell wall material to avoid numerical problems; therefore, the bending moment never reaches a saturated value, but continuously increases with further macroscopic rotation (see Fig. 15). Similar to B/B_{class}, $\sigma_{y\_bending}/\sigma_{\text{bulk}}$ increases with increasing H/d, but in this case a converged value is obtained relatively fast, for $H/d \geqslant 8$. Note that $\sigma_{y\_bending}$ converges to $\approx 0.7\sigma_{\text{bulk}}$, not to σ_{bulk} itself. This is due to the fact that $\sigma_{y\_bending}$ bending represents the yield stress value at the onset of the transition from elastic to plastic bending, i.e. at the elastic limit. As can be observed from Fig. 4, this occurs at approximately 0.7 times the peak stress value.

Fig. 17 shows the equivalent strain distribution for a sample with $H/d = 10$, at an applied rotation of (a) $\theta = \frac{\pi}{12}$, (b) $\theta = \frac{\pi}{6}$, and (c) $\theta = \frac{\pi}{4}$. The deformation starts to localize in cells closest to the top and bottom boundaries – i.e., furthest from the neutral axis – in the nonlinear transition zone, see Fig. 17a. Initially, there are several deformation regions with a thickness of ~ 2 cells, with more or less equal strain concentration. With further macroscopic rotation of the sample, some of the bands become more active than others and extend towards the neutral axis, while their thicknesses increase (see Fig. 17b). A plastic hinge gradually forms at a location along the beam where the most active zones are present (see Fig. 17b), and it starts to act as a pivot for the rotation of the beam (see Fig. 17c). After the plastic hinge formation, the deformation localizes even more in the already active bands, while in the remainder of the beam the strain level does not increase much (compare Figs. 17b and c).

Fig. 18 shows: (a) ε_{11}, (b) ε_{22}, and (c) ε_{12max} distribution for the same Voronoi sample analyzed in Fig. 17, and for $\theta = \frac{\pi}{6}$. Note that, as in compression, ε_{12max} is the shear strain plotted with respect to a 45° counter-clockwise rotated reference frame. A comparison of the strain maps in Fig. 18 with the corresponding strain maps under compression, Fig. 7, reveals that the strain localization under bending occurs through a similar mechanism as under compression: localized bands initiate at weak cells, and propagate in the maximum shear direction through distortion and rotation of the neighboring cells.

4. Discussion

Bart-Smith et al. [13] performed compression tests with X-ray computed tomography on Alporas foams, and concluded that cells exhibiting severe deformation within localization bands have either of the two following morphologies: (1) ellipsoidal cells with T-shaped cell-wall intersection; (2) non-planar cell-walls with appreciable curvature (see also Dannemann and Lankford [14], Hakamada et al. [15], Park and Nutt [16], Wang et al. [17], McCullough et al. [47]). The second morphology has not been included in the 2D Voronoi microstructures studied in this paper.[7] Fig. 19a shows a highly deformed cell from a Voronoi sample under compression (line A–A in Fig. 7a intersects this cell, which is on the first localization band from the bottom boundary). Although the cell is not elliptical, it is not equiaxed either, and it has a T-shaped cell-wall intersection (the junction point enclosed by a square) similar to the first morphology described in Bart-Smith et al. [13]. Because they are constrained by the surrounding cells, such "*weak*" cells cannot deform in an isolated manner; instead, they activate a band of highly deforming cells that propagates in the energetically most preferable direction, i.e. the direction of maximum shear strain for the case of Voronoi microstructures (see Fig. 7e). Cells located in deformation bands deform mainly by distortion combined with rotation, and cells adjacent to these bands undergo a pure rigid body rotation to accommodate their highly deforming neighboring cells (mechanisms X and Y in Fig. 8, respectively). Rigid body rotation zones can be clearly seen by comparing Figs. 7e and 7g (also Figs. 7f and h); they correspond to the regions where $-\omega_{12}$ is maximum (green circular regions in Fig. 7g), and ε_{12max} is much lower in between the localized deformation bands (Fig. 7e). Bastawros et al. [10] pointed towards three major deformation mechanisms at the cell-level, which trigger band formation in closed-cell aluminum (Alporas) foams under uniaxial compression: (1) only distortion; (2) distortion plus rotation; and (3) distortion plus in-plane shear. In the 2D Voronoi model, only the second one, denoted as X in Fig. 8, is observed. Moreover, in the Alporas foams, the deformation

[7] The reader is referred to Chen et al. [37], Tekoğlu [41], Grenestedt [48], Simone and Gibson [49] for modeling studies on the effects of cell wall wiggles and curvature.

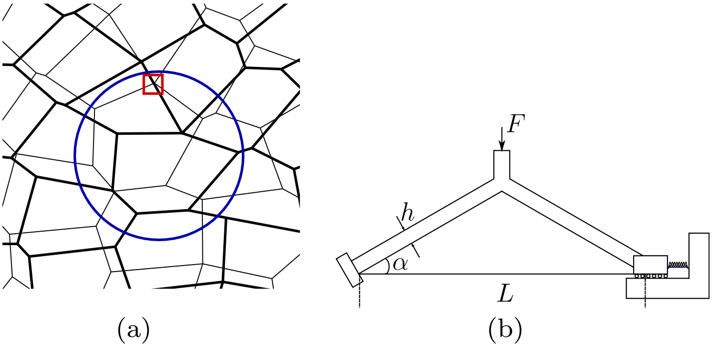

Fig. 19. (a) Deformation of a "*weak*" cell. (b) The configuration demonstrating the important parameters in yielding of a "*weak*" (elliptical) cell (see also Fig. 7 in Bart-Smith et al. [13]).

band normals are usually within ~20° of the loading direction, only rarely reaching ~40°, whereas it is usually ~45° for Voronoi samples.

The Voronoi model and experiments on metal foams Andrews et al. [11], Jeon and Asahina [12] agree in the fact that decreasing sample size leads to decreasing stiffness (see Fig. 5a), although the effect of the sample size is lower for the experiments of Jeon and Asahina [12] on the defect-free Alporas foams (see Fig. 3a). In case of elastic deformation, size effects can be explained by weak boundary layers located near the stress-free boundaries (left and right boundaries for the sample shown in Fig. 7), with a thickness of ~1 or 2 cell sizes. The cells located at or near these boundaries are more compliant compared to those located in the bulk, which are surrounded (and therefore, restricted) by other cells. The thickness of the weak boundary layers does not depend on the sample size, meaning that their area fraction increases with decreasing sample size, which results in a decrease in the effective stiffness of the specimens (see also Tekoğlu [41], Tekoğlu and Onck [42], Onck et al. [44], Tekoğlu and Onck [50]). In case of plasticity, comparing the results of Andrews et al. [11] and Jeon and Asahina [12] on Alporas foams – with and without structural defects, respectively – it can be concluded that the weak boundary layers do not play an important role, and the size effects are primarily introduced by structural defects. In Bastawros et al. [10], it is shown that the localized deformation bands initiate at the onset of the nonlinear response, at a stage prior to the onset of the plateau stress (corresponding to the peak stress in this study). With further deformation, new collapse bands form in neighboring regions to the previously formed bands, during which the overall stress in the sample remains more or less constant at the plateau level. This suggests that the macroscopic yielding of a sample is initiated by the formation of the first band; the sooner the deformation localizes in a band in a sample, the lower the yield strength of that sample. The schematic in Fig. 19b (see also Fig. 7 in Bart-Smith et al. [13]) shows the four important parameters which closely relate to the deformation of a cell: cell-wall thickness over cell-width (h/L), the angle α, the force F acting on the T-shaped cell-wall intersection, and the boundary condition acting on the node at the right side of the cell. If this node is clamped, the cell yields under a smaller force F for a smaller α (i.e., a more elliptical cell) and a smaller h/L (i.e., a smaller density). For the other extreme case, i.e. if this node is free to displace horizontally, α has a negligible effect on the deformation of the cell (for a detailed limit load analysis, see [13]). Note that for 3D cellular solids as well as 2D Voronoi samples, this boundary condition is not well defined; it can be thought of as a constraint imposed by the surrounding cells. Structural defects increase the density of weak cells by decreasing the angle α. If the sample size is small, the cells with defects are weaker: even if a weak cell is located in the middle of a sample, there are only a few cells between the weak cell and the stress-free boundaries (meaning the right-end node in Fig. 19b is less constrained) and consequently, the weak cell deforms more easily. Removing structural defects decreases the weak cell density, therefore prevents early localization band formation, and avoids size effects. Even though no structural defects are introduced into the 2D Voronoi model, cells such as the one shown in Fig. 19a act as defects, which leads to size effects. The enhanced sensitivity of the weak Voronoi cells to the presence of free-edges might be attributed to the absence of 3D constraints in the 2D standing of cells.

It is, however, possible to obtain a size-independent plastic response for 2D perfect hexagonal honeycombs (see Onck et al. [44]), where there are no cells that yield earlier under the same loading condition.

Fig. 11, showing the strain distribution in a Voronoi sample, clearly points out the origin of the size effects under shear. Both in the Voronoi model and in experiments, the rotational degrees of freedom of the cell-walls connected to the top and bottom boundaries (i.e., bonded to the rigid loading platens) are fully constrained. Consequently, low rotational zones – which could be thought of as strong boundary layers – extending over $\sim$1 or 2 cells form near these boundaries. Although the thickness of the strong boundary layers differs slightly from one sample to another due to the stochastic nature of cell size/shape distribution, it remains almost the same independent of the sample size. Therefore, the area fraction of these strong boundary layers is larger for smaller samples, leading to an increase in both stiffness and strength. With increasing sample thickness, on the contrary, the contribution from the strong boundaries decreases, eventually vanishing for $H/d > \sim 2$ in closed-cell Alporas foams, and for $H/d > \sim 8$ in the Voronoi samples. The increase in shear strength with decreasing sample height is also shown by Onck et al. [44] for regular hexagons, by Chen and Fleck [18], and Diebels and Steeb [45] for perturbed hexagons, respectively. The strengthening is least pronounced for perfect hexagons and most pronounced for Voronoi microstructures.

For Voronoi samples under compression, localized deformation bands initiate at weak cells randomly distributed around the sample. For indentation, however, the indenter edges trigger early plastic shear strain localization. The strain concentrations at the two edges of the indenter set the starting points between which the localization bands must develop. Further straining proceeds by crushing of these discrete bands located just below the indenter (see Fig. 14). With decreasing indenter size, i.e. the two indenter edges approaching each other, the volume of material to be deformed decreases as well, reducing the number of weak cells that can trigger localization band formation (compare Figs. 14c and d). Moreover, for a smaller plastically deforming zone under the indenter, there are fewer surrounding cells to elastically accommodate its deformation, i.e. the plastically deforming zone is more constrained. These combined effects cause the indentation peak stress to increase with decreasing indenter size. The increasing scatter with decreasing indenter size in Fig. 13 can be explained by the difficulty of finding a unique deformation path for smaller material volumes under the indenter.

Bending of a 2D Voronoi microstructure corresponds to the compression and tension of the two sides of the sample separated by the neutral axis. The only additional effect in bending is that there is a gradient in compressive and tensile strains, and therefore weak boundary layers at the top and bottom free-edges are subjected to larger strains than the bulk of the sample. This seems to have no effect on the cell deformation mechanisms: strain maps for the compression and bending, Figs. 7 and 18, respectively, show that localization bands initiate and propagate through the same mechanisms in both cases. However, due to the strain gradients, the contribution of the weak boundary layers to the sample response is larger in bending than in compression, and this leads to a larger reduction in the effective mechanical properties.

The results for all four boundary value problems show that the size-dependent mechanical behavior of 3D real foams is successfully represented by the 2D Voronoi diagrams, although some of the underlying deformation mechanisms could not be observed for the 2D samples. A major difference between the 2D honeycombs and 3D foams is the dependence of the bulk properties on the relative density: Young's modulus E_{bulk} varies with relative density power 3 for 2D samples, but power 2 for foams, and strength σ_{bulk} varies with relative density power 2 for 2D samples, but power 1.5 for foams. In the current study we eliminate most of this effect by normalizing the results with respect to the bulk properties. Another important difference between the Voronoi model and the 3D foams is the plastic Poisson ratio, which could be defined as $\nu^p = -\varepsilon_{11}/\varepsilon_{22}$. Low density Alporas foams ($\rho < 0.1$) have a plastic Poisson ratio around zero (see e.g. Bastawros et al. [10] and Deshpande and Fleck [39]), but for the 2D Voronoi microstructures we find $\nu^p > 0.5$, as can be deduced by comparing the strain maps for ε_{11} and ε_{22} (see Fig. 7). The macroscopic Poisson ratio ν^p for a Voronoi diagram is calculated using the following expression

$$\nu^p = \frac{\sum_{i=1}^{n} A_i \nu_i^p}{\sum_{i=1}^{n} A_i}, \tag{3}$$

where A_i is the area of a triangle used in the strain mapping procedure (see Fig. 2), $\nu_i^p = -(\varepsilon_{11}/\varepsilon_{22})_i$ the value of the Poisson ratio in that triangle, and n the total number of triangles for that Voronoi diagram. Applying the definition in (3) in the linear elastic range yields an elastic Poisson ratio of slightly less than 1, see also Gibson and Ashby [34] and Tekoğlu and Onck [42], and the Poisson ratio decreases with applied strain to approximately 0.5 in the plastic regime. One should also note that the ratio of the stress-free boundary layers (for compression and bending) or constrained layers (for shear and indention) to the entire cross-section under loading is not the same in 2D and 3D. For example, for a 2D uniaxial compression sample with an edge length L and a stress-free boundary layer of thickness a at each side, this ratio is $2a/L$, whereas for a 3D sample with a square cross-section the ratio is $4a(L-a)/L^2$. In addition, the microstructural defects inherent to Alporas foams (e.g. partially coupled cells, missing cells, and collapsed cells) are not accounted for in the Voronoi model. These microstructural differences and the fact that real foams are subjected to additional 3D constraint effects partly explain the differences between the model and the experiments.

5. Summary and conclusions

Mechanical properties of cellular solids show a strong size-dependence in length scales when the cell size is of the order of the specimen size. In order to elucidate the origin of these size effects, four key structural engineering problems (compression, shear, indentation, and bending) are solved on 2D Voronoi model materials, mimicking the cellular morphology of random foams. It is shown that the effective mechanical properties of the Voronoi samples gradually change with increasing sample size, until the point where the structural dimensions of the samples are large enough to include many cells. These size effects can be traced back to typical deformation modes associated with cellular morphology, i.e. the formation of localized deformation bands in regions containing "*weak*" cells. Fig. 20 shows

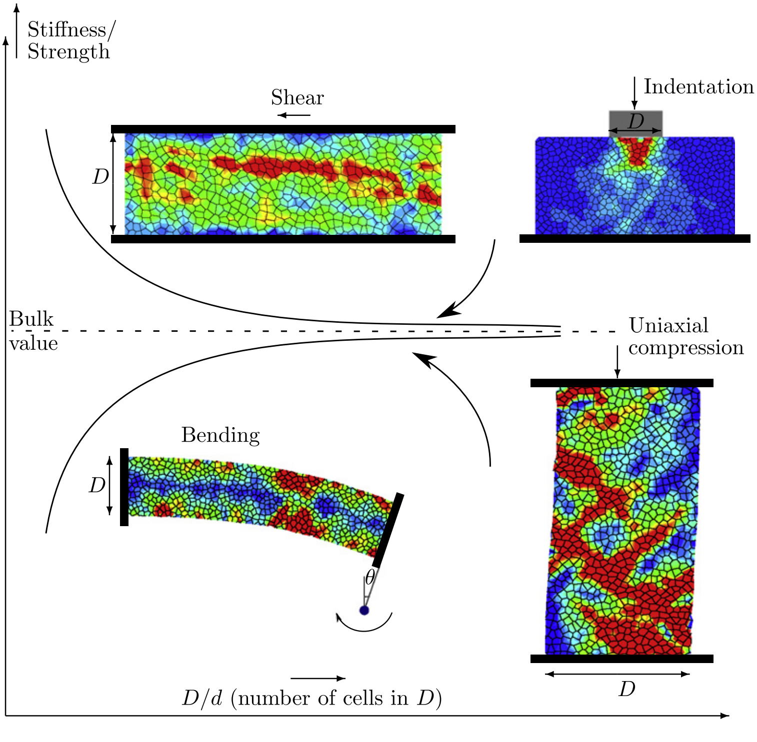

Fig. 20. The deformation patterns and size effects observed for the 2D Voronoi samples under loading conditions analyzed in this paper.

typical deformation patterns under each loading condition analyzed in this study, while schematically presenting the observed size effects:

- Under compression, the stiffness and strength of the Voronoi samples decrease with decreasing sample size. The reduction in the stiffness is associated with the increased area fraction of weak boundary layers located at the stress-free edges, in which the cells are more compliant compared to the cells in the bulk. In case of plastic deformation, the weak cells with a T-shaped cell-wall intersection (see Fig. 19a) trigger the formation of localized deformation bands. In case of small samples, weak cells close to the stress-free edges experience a lower constraint of the surrounding cells, accelerating localization. Therefore, the smaller the sample size the easier the band formation, and the lower the plastic strength.
- For shear, low rotational zones of ~1 or 2 cell sizes form at the boundaries where the samples are bonded to rigid loading platens, and act as strong boundary layers with a larger resistance to deformation. The area fraction of these strong boundary layers increases with decreasing sample size, leading to an increase in both the stiffness and strength of the samples.
- In indentation, the deformation is mainly confined to a zone under the indenter, in which localization bands that connect the two edges of the indenter form. For a small indenter size, the volume of loaded material under the indenter is small, decreasing the number of weak cells that can activate band formation and enhancing the elastic constraint. This causes an increase in the indentation strength with decreasing sample size.
- The strain localization in bending occurs through similar mechanisms as under compression. The difference is that in bending the tensile and compressive strains increase when moving away from the neutral axis, as a result of which the weak boundary layers located at the stress-free edges have an enhanced contribution to the mechanical response compared to the cells located in the bulk. This causes the reduction in effective mechanical properties to be larger in bending than in compression.

Acknowledgements

Cihan Tekoğlu gratefully acknowledges the support of the inter-university attraction poles (IAP) Programme P6/24, funded by the Belgian State, Belgian Science Policy, as well as the support of the FNRS, Belgium, through a post-doctorate grant related to a HETMAT network project.

References

[1] Lakes RS. Size effects and micromechanics of a porous solid. J Mater Sci 1983;18:2572–80.
[2] Lakes RS. Experimental microelasticity of two porous solids. Int J Solids Struct 1986;22:55–63.
[3] Brezny R, Green DJ. Characterization of edge effects in cellular materials. J Mater Sci 1990;25:4571–8.
[4] Anderson WB, Chen CP, Lakes RS. Experimental study of size effects and surface damage in closed-cell polymethacrylimide and open-cell copper foams. Cell Polym 1994;13:1–15.
[5] Anderson WB, Lakes RS. Size effects due to Cosserat elasticity and surface damage in closed-cell polymethacrylimide foam. J Mater Sci 1994;29:6413–9.
[6] Bart-Smith H, Hutchinson JW, Evans AG. Measurement and analysis of the structural performance of cellular metal sandwich construction. Int J Mech Sci 2001;43:1945–63.
[7] Bart-Smith H, Hutchinson JW, Fleck NA, Evans AG. Influence of imperfections on the performance of metal foam core sandwich panels. Int J Solids Struct 2002;39:4999–5012.
[8] Crupi V, Montanini R. Aluminium foam sandwiches collapse modes under static and dynamic three-point bending. Int J Impact Eng 2007;34:509–21.
[9] Styles M, Compston P, Kalyanasundaram S. The effect of core thickness on the flexural behaviour of aluminium foam sandwich structures. Compos Struct 2007;80:532–8.
[10] Bastawros AF, Bart-Smith H, Evans AG. Experimental analysis of deformation mechanisms in a closed-cell aluminum alloy foam. J Mech Phys Solids 2000;48:301–22.
[11] Andrews EW, Gioux G, Onck P, Gibson LJ. Size effects in ductile cellular solids. Part II: experimental results. Int J Mech Sci 2001;43:701–13.
[12] Jeon I, Asahina T. The effect of structural defects on the compressive behavior of closed-cell Al foam. Acta Mater 2005;53:3415–23.
[13] Bart-Smith H, Bastawros AF, Mumm DR, Evans AG, Sypeck DJ, Wadley HNG. Compressive deformation and yielding mechanisms in cellular Al alloys determined using X-ray tomography and surface strain mapping. Acta Mater 1998;46:3583–92.

[14] Dannemann KA, Lankford J. High strain rate compression of closed-cell aluminium foams. Mater Sci Eng A 2000;293:157–64.
[15] Hakamada M, Kuromura T, Chino Y, Yamada Y, Chen Y, Kusuda H, et al. Monotonic and cyclic compressive properties of porous aluminum fabricated by spacer method. Mater Sci Eng A 2007;459:286–93.
[16] Park C, Nutt SR. Anisotropy and strain localization in steel foam. Mater Sci Eng A 2001;299:68–74.
[17] Wang J, Sun W, Anand S. A microstructural analysis for crushable deformation of foam materials. Comput Mater Sci 2008;44:195–200.
[18] Chen C, Fleck NA. Size effects in the constrained deformation of metallic foams. J Mech Phys Solids 2002;50:955–77.
[19] Rakow JF, Waas AM. Size effects and the shear response of aluminum foam. Mech Mater 2005;37:69–82.
[20] Kesler O, Gibson LJ. Size effects in metallic foam core sandwich beams. Mater Sci Eng A 2002;326:228–34.
[21] Stupak PR, Donovan JA. Deformation and energy absorption of polymer foams as a function of 2-D indenter and absorber geometries. Polym Eng Sci 1994;34:857–64.
[22] Prakash O, Sang H, Embury JD. Structure and properties of Al–SiC foam. Mater Sci Eng A 1995;199:195–203.
[23] Kumar PS, Ramachandra S, Ramamurty U. Effect of displacement-rate on the indentation behavior of an aluminum foam. Mater Sci Eng A 2003;347:330–7.
[24] Ramachandra S, Sudheer Kumar P, Ramamurty U. Impact energy absorption in an Al foam at low velocities. Scripta Mater 2003;49:741–5.
[25] Ramamurty U, Kumaran MC. Mechanical property extraction through conical indentation of a closed-cell aluminum foam. Acta Mater 2004;52:181–9.
[26] Kádár C, Maire E, Borbély A, Peix G, Lendvai J, Rajkovits Z. X-ray tomography and finite element simulation of the indentation behavior of metal foams. Mater Sci Eng A 2004;387–389:321–5.
[27] Mohan K, Yip TH, Sridhar I. Effect of face sheet material on the indentation response of metallic foams. J Mater Sci 2007;42:3714–23.
[28] Lu G, Shen J, Hou W, Ruan D, Ong L. Dynamic indentation and penetration of aluminium foams. Int J Mech Sci 2008;50:932–43.
[29] Olurin OB, Fleck NA, Ashby MF. Indentation resistance of an aluminium foam. Scripta Mater 2000;43:983–9.
[30] Antoniou A, Onck PR, Bastawros AF. Experimental analysis of compressive notch strengthening in closed-cell aluminum alloy foam. Acta Mater 2004;52:2377–86.
[31] Mora R, Waas AM. Measurement of the Cosserat constant of circular-cell polycarbonate honeycomb. Philos Mag A 2000;80:1699–713.
[32] Guo XE, Gibson LJ. Behavior of intact and damaged honeycombs: a finite element study. Int J Mech Sci 1999;41:85–105.
[33] Zhu HX, Thorpe SM, Windle AH. The geometrical properties of irregular two-dimensional Voronoi tessellations. Phil Mag A 2001;81:2765–83.
[34] Gibson LG, Ashby MF. Cellular solids: structure and properties. Cambridge: Cambridge University Press; 1997.
[35] Andrews EW, Gibson LJ. The role of cellular structure in creep of two-dimensional cellular solids. Mater Sci Eng A 2001;303:120–6.
[36] Zhu HX, Hobdell JR, Windle AH. Effects of cell irregularity on the elastic properties of open-cell foams. Acta Mater 2000;48:4893–900.
[37] Chen C, Lu TJ, Fleck NA. Effect of imperfections on the yielding of two-dimensional foams. J Mech Phys Solids 1999;47:2235–72.
[38] Gioux G, McCormack TM, Gibson LJ. Failure of aluminum foams under multiaxial loads. Int J Mech Sci 2000;42:1097–117.
[39] Deshpande VS, Fleck NA. Isotropic constitutive models for metallic foams. J Mech Phys Solids 2000;48:1253–83.
[40] Doyoyo M, Wierzbicki T. Experimental studies on the yield behavior of ductile and brittle aluminum foams. Int J Plast 2003;19:1195–214.
[41] Tekoğlu C. Size effects in cellular solids. Groningen, The Netherlands: University of Groningen; 2007. <http://dissertations.ub.rug.nl/faculties/science/2007/c.tekoglu/>.
[42] Tekoğlu C, Onck PR. Size effects in two-dimensional Voronoi foams: a comparison between generalized continua and discrete models. J Mech Phys Solids 2008;56:3541–64.
[43] Alkhader M, Vural M. Mechanical response of cellular solids: role of cellular topology and microstructural irregularity. Int J Eng Sci 2008;46:1035–51.
[44] Onck PR, Andrews EW, Gibson LJ. Size effects in ductile cellular solids. Part I: modeling. Int J Mech Sci 2001;43:681–99.
[45] Diebels S, Steeb H. The size effect in foams and its theoretical and numerical investigation. Proc R Soc Lond A 2002;458:2869–83.
[46] Onck PR. Scale effects in cellular metals. MRS Bull 2003;28:279–83.
[47] McCullough KYG, Fleck NA, Ashby MF. Uniaxial stress–strain behaviour of aluminium alloy foams. Acta Mater 1999;47:2323–30.
[48] Grenestedt JL. Influence of wavy imperfections in cell walls on elastic stiffness of cellular solids. J Mech Phys Solids 1998;46:29–50.
[49] Simone AE, Gibson LJ. The effects of cell face curvature and corrugations on the stiffness and strength of metallic foams. Acta Mater 1998;46:3929–35.
[50] Tekoğlu C, Onck PR. Size effects in the mechanical behavior of cellular materials. J Mater Sci 2005;40:5911–7.